scientific reports

Check for updates

OPEN

Toward a mechanistic characterisation of marine heatwaves

Zijie Zhao[1,2,17], Neil J. Holbrook[2,3,17]✉, Antonietta Capotondi[4,5], Sophie Cravatte[6,7], Jules B. Kajtar[8], Alex Sen Gupta[9,10], Erik Behrens[11], Martina A. Doblin[12,13], Ming Feng[14], Andrew E. Kiss[15] & Claire M. Spillman[16]

A mechanistic understanding of marine heatwaves (MHWs) requires robust frameworks for detection, tracking, and attribution. Conventional pointwise definitions, which identify MHWs pixel by pixel relative to fixed thresholds, have enabled global analyses but neglect the event-scale spatiotemporal evolution and underlying drivers. Recent kinematic approaches overcome the evolution issue by treating MHWs as evolving spatiotemporal objects. Here, we build on this framework by also considering the drivers. We examine the MHW dynamics by quantifying the scale and driver dependence of MHW objects, identifying dominant forcing mechanisms throughout their lifetimes, and characterising key features linked to distinct drivers. We further introduce a normalisation framework that preserves the event scale, while enabling composite analyses across multiple MHWs. Applying this approach to the Tasman Sea, a region of complex atmosphere–ocean interactions, we reveal distinct atmospheric and oceanic conditions that shape the MHW evolution at different stages. By explicitly linking evolving MHW entities to their physical drivers, our method advances the mechanistic characterisation of MHWs, enhances understanding of their spatiotemporal dynamics, and informs prospects for improved prediction.

Marine heatwaves (MHWs[1–3]) are discrete and prolonged warm ocean temperature extremes that can have profound ecological, climatic, and socioeconomic impacts. These events have garnered significant attention in recent years due to their increasing frequency, intensity, and duration[4], largely attributed to anthropogenic climate change[5–12]. Impacts from MHWs can include widespread coral bleaching, loss of kelp and seagrass, shifts in species distributions, declines in fisheries, and disruptions to marine ecosystems, with cascading effects on human communities that rely on these ecosystem services and resources[13–16]. Iconic examples include the 2011 marine heatwave off Western Australia, which resulted in extensive loss of kelp forests[17,18] and seagrass meadow[19], while the northeast Pacific "Blob" event that occurred from 2014 to 2016 led to substantial decreases in phytoplankton biomass[20], and devastating impacts on higher trophic level species[21].

A mechanistic understanding of MHWs not only requires a suitable MHW definition for their detection, but also an effective characterisation of their causality. Much of our recent understanding of MHWs has been enabled by a commonly used statistical definition[1], which defines MHWs as discrete warm ocean temperature extremes, persisting for at least five days above a seasonally varying 90th percentile threshold, relative to a fixed climatological period[22]. This definition is easy to apply, and when used with near-global satellite sea surface temperature data, allows wide adoption by providing comparable and interpretable event metrics across space

[1]Department of Earth System Science, University of California Irvine, Irvine, CA, USA. [2]Institute for Marine and Antarctic Studies, University of Tasmania, Hobart, TAS, Australia. [3]ARC Centre of Excellence for Climate Extremes, University of Tasmania, Hobart, TAS, Australia. [4]Cooperative Institute for Research in Environmental Sciences, University of Colorado Boulder, Boulder, CO, USA. [5]NOAA/Physical Sciences Laboratory, Boulder, CO, USA. [6]LEGOS, Université de Toulouse, IRD, CNES, CNRS, UPS, Toulouse, France. [7]IRD, Nouméa, New Caledonia. [8]National Oceanography Centre, Southampton, UK. [9]Climate Change Research Centre & Centre for Marine Science and Innovation, The University of New South Wales, Sydney, NSW, Australia. [10]ARC Centre of Excellence for Antarctic Science, The University of New South Wales, Sydney, NSW, Australia. [11]Earth Sciences New Zealand, Wellington, New Zealand. [12]University of Technology Sydney, Ultimo, NSW, Australia. [13]Sydney Institute of Marine Science, Mosman, NSW, Australia. [14]CSIRO Environment, Indian Ocean Marine Research Centre, Crawley, WA, Australia. [15]Research School of Earth Sciences and ARC Centre of Excellence for Climate Extremes, Australian National University, Canberra, ACT, Australia. [16]Bureau of Meteorology, Docklands, VIC 3008, Australia. [17]Zijie Zhao and Neil J. Holbrook co-lead of the research and share the first authorship. ✉email: neil.holbrook@utas.edu.au

and time. While this definition has broad applicability and appeal, it does not take into account the spatial scale of these events, their evolution in space and time, or their causality.

To address these limitations, some recent studies have considered the evolving nature of MHWs by shifting from a Eulerian framework (where temporal MHW changes are examined at fixed locations in space) to space–time evolving semi-Lagrangian approaches (where MHW characteristics are examined in a moving frame of reference). One approach uses spatially incoherent semi-Lagrangian methods, in which three-dimensional (3D; two spatial dimensions and time) MHW entities are identified by linking spatiotemporally connected grid cells across time[23–25] (Supplementary Table S1). However, this approach does not ensure spatial connectivity of MHW structures at each time step. Alternatively, spatially coherent methods first identify two-dimensional (2D) MHW objects as spatially contiguous regions in latitude–longitude, and then track them over time to construct 3D entities[26,27] (Supplementary Table S1). Spatial coherence is maintained at each time step by applying an overlap criterion between MHW objects in successive time steps. Studies employing these semi-Lagrangian methods have demonstrated their ability to effectively describe the spatiotemporal evolution of MHWs, including their phases of growth and decay, and intricate kinematics like splitting and merging. While these approaches have increased our understanding of MHW evolution, they nevertheless remain statistical representations of MHWs, as each MHW exhibits unique spatiotemporal variability that is difficult to capture through composite analyses on fixed grids. Moreover, previous analyses do not align tracked MHW entities with physically coherent structures in atmospheric and oceanic variables associated with local drivers, limiting their utility to statistical characterisation rather than enabling a dynamical understanding of MHWs from a moving-object perspective.

The goal of this paper is to develop an approach that not only kinematically detects MHWs as evolving objects in space and time, but that also dynamically characterises these MHW objects by their dominant drivers evaluated through an evolving temperature budget analysis in a moving frame of reference. Our approach connects MHW characteristics in a scale-dependent semi-Lagrangian framework (as 3D spatiotemporally evolving entities formed by temporally connecting 2D spatial objects) with their key local drivers, focusing on air-sea heat fluxes and oceanic advection[2,28], which represents an important step toward a mechanistic characterisation of MHWs. Focusing our analysis on the Tasman Sea as a case study region, and as an exemplar of ocean dynamic complexities where eddies can be very important, we first examine metrics of MHW entities tracked under varying spatial scales. We then determine the dominant driver across each MHW entity through its lifetime and analyse MHW temperature budget evolutions and metrics with driver dependency. A novel approach is then introduced to capture the evolution of these MHW objects in time and space by scaling their spatiotemporal extent into a normalised framework, such that different events with varying spatiotemporal scales can be effectively compared and examined from a composite perspective. Using this approach, background conditions during MHWs under certain local drivers, specifically air-sea heat fluxes and oceanic advection, are summarised throughout the MHW lifespans, overcoming the difficulties of conducting dynamical assessments of moving MHW objects that were generally faced in previous studies.

Results

A key aspect of MHW objects is their spatial scale, which is closely associated with their dominant drivers. Tracking MHW entities requires a choice of the spatial scales to be tracked (see methods)—noting that the associated smoothing may modify the shape and size of the original objects, and therefore the grid cell MHW metrics contained within each object. This leads to spatiotemporal MHW patterns that may differ from those derived using fixed-grid approaches, thus representing MHWs under varying spatial scales.

MHWs in the Tasman Sea exhibit pronounced spatial variability from a Eulerian Perspective. Within the East Australian Current (EAC) Extension, in the southwest Tasman Sea, frequent, intense, but short-lived MHWs occur, driven by the southward flow of the mean EAC and substantial eddy activity[29–31] (Supplementary Fig. S1). In contrast, the open ocean and coastal waters around New Zealand experience less frequent, weaker (on average), but more persistent MHWs. This stark contrast between the EAC boundary current region and the open ocean highlights the potential coexistence of spatially coherent, large-scale warming patterns and smaller, spatially fragmented events shaped by intensified warm water transports associated with mesoscale eddies[31]. As such, the Tasman Sea provides a useful case study region for examining how spatial scales influence MHW detection and characterisation.

As the minimum spatial scale of tracked MHW entities increases (Fig. 1), discrepancies between the fixed-grid and tracked MHW signals become larger, leading to an evident elimination of small-scale MHW occurrences after smoothing. For instance, applying a 2.5° spatial smoothing reduces the annual MHW days by more than 50% in the EAC and its Extension regions compared to raw MHW outputs, whereas the reduction is less pronounced near New Zealand (Fig. 1f). This regional difference reflects the stronger influence of oceanic eddy activity and mesoscale perturbations on MHWs in the East Australian Current and its extension[29–33], generating many localised features that are progressively filtered out as the smoothing scale increases. In contrast, MHWs near New Zealand are primarily influenced by air-sea heat fluxes associated with large-scale atmospheric circulation[34–36], such as high-pressure systems, making them less sensitive to spatial filtering. The influence of spatial scale is evident across time, with the annual proportion of ocean area classified as experiencing MHWs consistently decreases as spatial scale increases (Fig. 1g).

Tracked MHW entities exhibit characteristics defined over their full spatiotemporal lifespans, which cannot be reliably inferred from MHWs identified within isolated grid cells. Here, we present the probability distributions of key MHW entity metrics, including duration, maximum intensity, area, and displacement (Fig. 2). Definitions of these metrics are provided in the Methods (and Supplementary Table S2). Except for maximum intensity, these metrics are not normally distributed but are strongly skewed by short-lived (Fig. 2a), small-scale (Fig. 2c), and weakly propagating (Fig. 2d) events. The duration distribution appears relatively insensitive to changes in spatial scale, likely arising from a balance between the merging of small-scale events into larger, longer-lived

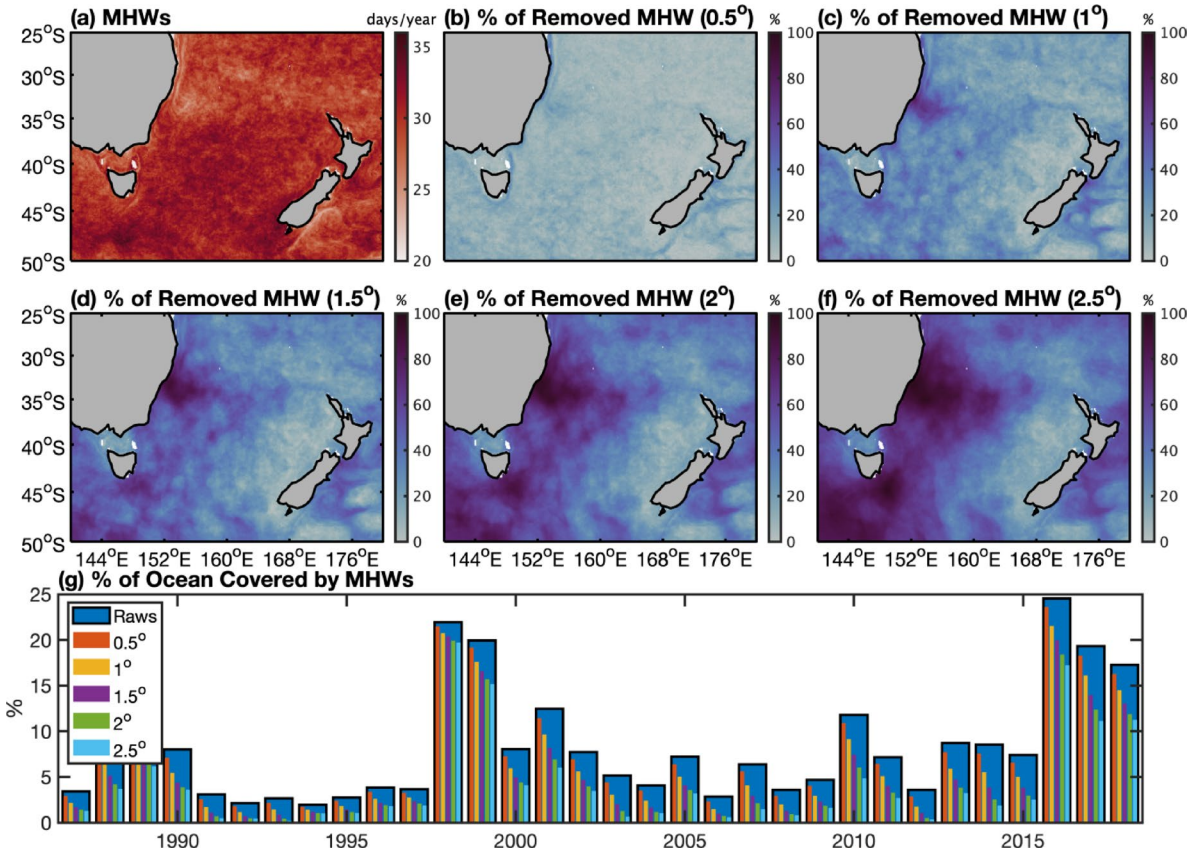

Fig. 1. Marine heatwave occurrences (days/year) in the Tasman Sea at different spatial scales. (**a**) Annual MHW occurrences detected using a fixed-grid method. (**b**–**f**) Percentage of MHW events excluded when restricting detection to specific spatial scales (0.5° and larger, to 2.5° and larger). (**g**) Time series of the annual percentage of Tasman Sea area affected by MHWs, comparing fixed-grid and scale-dependent detection results. In the legend, 'Raws' identifies the percentage of ocean covered by MHWs based on a fixed grid, pixel-based analysis.

structures and the filtering out of persistent, isolated small-scale features. As the minimum spatial scale used for tracking increases, the duration distribution becomes less skewed, resulting in a longer mean duration (Fig. 2a). This shift likely reflects the removal of small-scale MHW features during the tracking process at coarser spatial scales. In contrast, the distribution of maximum intensity shows relatively little sensitivity to spatial filtering, although both the mean and median values from the 0.5° data are notably lower than those at coarser scales (e.g., 1.4° < 1.5°) (Fig. 2b). The maximum area of tracked MHW entities shows the greatest variation with spatial scale, with the mean and median increasing from 0.25×10^5 km^2 and 0.12×10^5 km^2 to 3.2×10^5 km^2 and 1.8×10^5 km^2, respectively (Fig. 2c). Note that the increase in MHW area with larger spatial scales arises not only from the removal of small-scale features, but also from their aggregation into larger events through the applied spatial smoothing, as evidenced by extremely large events that appear only at coarser spatial scales (Supplementary Fig. S2). Similarly, the distribution of maximum displacement shifts toward larger values as the spatial scale increases, consistent with the exclusion and merging of smaller MHW entities which have less potential for spatial propagation (Fig. 2d). Note that propagation measurements may be affected by splitting and merging events during tracking (see Methods). However, these processes involve only a small fraction of cases (< 15% across all spatial scales) and are therefore unlikely to substantially bias the overall estimates.

As detailed in the Methods, each MHW entity can be attributed to its dominant local driver. To assess the effect of the driver-based classification and investigate the temporal evolution of mixed-layer temperature budgets following the MHW entities driven by distinct local processes, we analysed the spatially averaged temperature budget evolution over the MHW lifespan. We focused on events primarily influenced by mixed-layer oceanic advection and net surface heat flux, which tend to be the most important terms for MHW onset and decay over large parts of the ocean[28]. For each event, spatially averaged temperature budget terms are normalised over 50 evenly spaced time steps from onset (0) to end (1) and composited according to their dominant driver across different spatial scales (Fig. 3).

During the lifespan of advection-dominated (ADV-dominated) MHWs, mixed-layer oceanic advection, characterised by anomalous horizontal temperature convergence in the mixed layer, is the primary contributor to upper-ocean warming throughout the event (Fig. 3a–e). As the MHW progresses, the "other terms" increasingly counteract this warming, contributing to its eventual decay, alongside the late-phase cooling effect

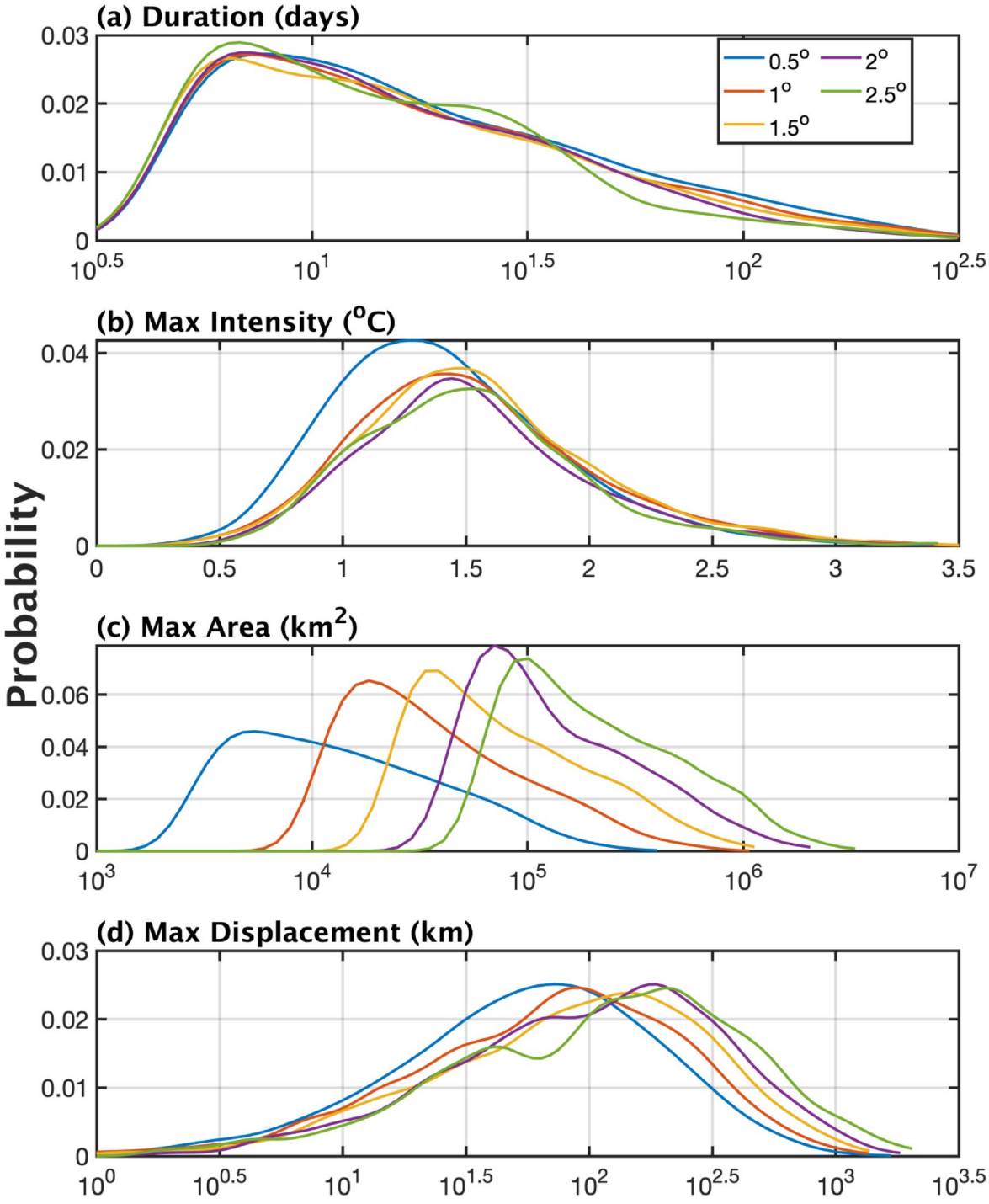

Fig. 2. Scale-dependent probability distributions of tracked MHW entity metrics. Probability density functions of (**a**) MHW duration (days), (**b**) maximum intensity (°C), (**c**) maximum area (km^2), and (**d**) maximum displacement (km) (see Methods), estimated using kernel density fitting, and corresponding to analyses at different spatial scales. Kernel density estimation was performed on the log-transformed metrics with a bandwidth of 0.1. Each curve represents a specific spatial scale. Total numbers of MHW entities for spatial scales 0.5–2.5° are 9,920, 3,577, 1,646, 856, and 528 events, respectively.

of oceanic advection. This evolution aligns with previous findings based on mean heat (or temperature) budget analyses during either the whole lifespan or the onset and decay phases of MHWs in western boundary current regions[37–39], where advection governs upper ocean temperature changes. In these regions, air-sea heat flux anomalies typically play a smaller role in upper ocean warming[37,38], owing to deep mixed layers favoured by a well-mixed upper ocean. From the composite perspective, the evolution of the temperature tendency budget in ADV-dominated MHWs shows pronounced spatial-scale dependence, characterised by earlier transitions

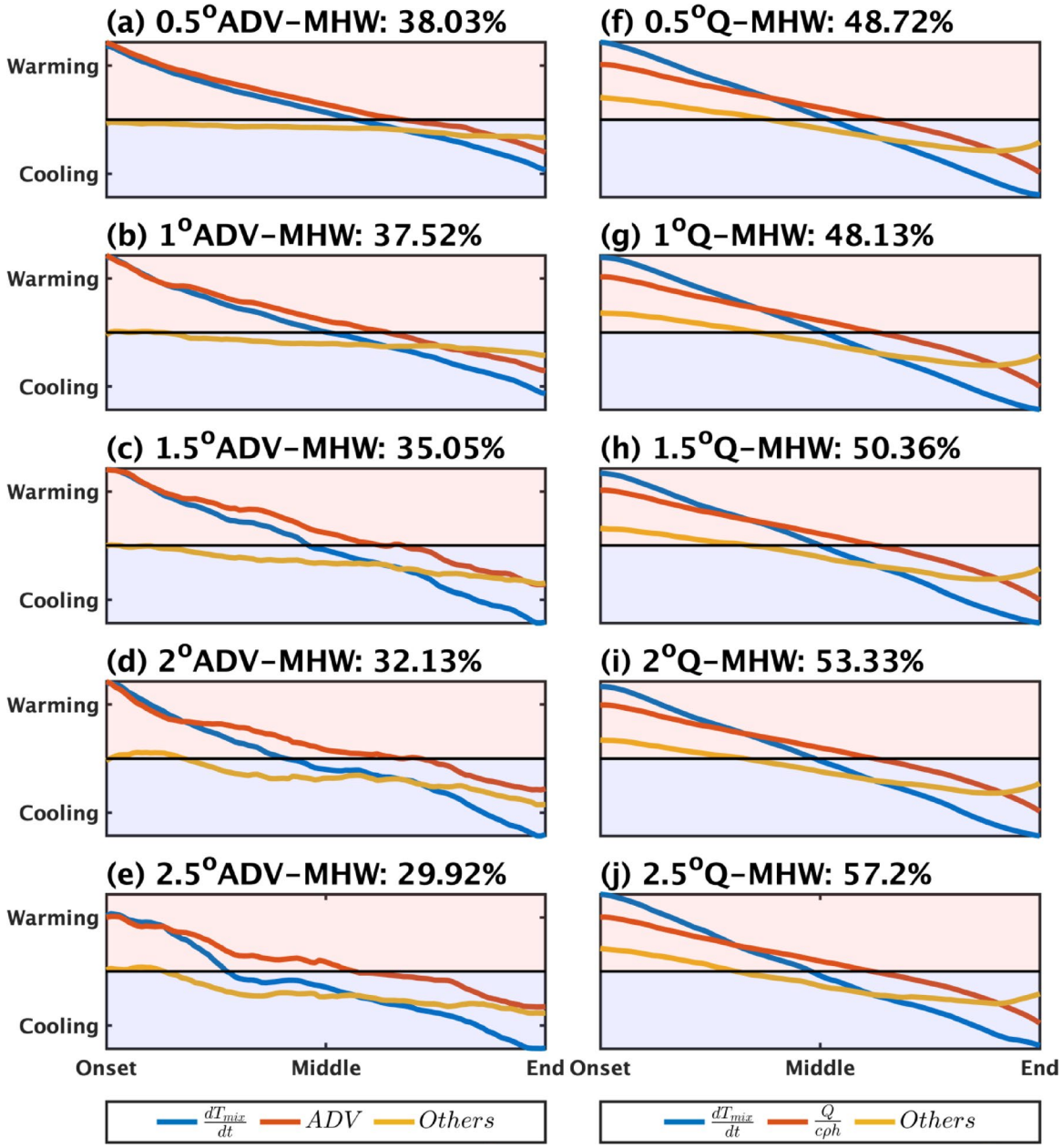

Fig. 3. Composite analysis of mixed-layer temperature tendency budgets for tracked MHW entities grouped by dominant local drivers Normalised temporal evolution (°C day^{-1}) of the ocean temperature tendency (blue), dominant local driver (red)—either the horizontal advection term (ADV) or surface heat flux term ($\frac{Q-Q_h}{c_p \rho h}$)—and the sum of remaining temperature budget terms (orange) are shown. All terms are spatially averaged over the domain of each individual MHW event at each time step, interpolated to a standardised 50-point timeline spanning the onset to termination of each event, and composited based on their identified dominant driver. (**a**–**e**) Composites for ADV-dominated MHWs with spatial smoothing scales from 0.5° to 2.5°. (**e**–**f**) Composites for Q-dominated MHWs over the same scale range. Proportions of corresponding MHW entities are labelled in the title of each panel. Total numbers of MHW entities for spatial scales 0.5–2.5° are 9,920, 3,577, 1,646, 856, and 528 events, respectively.

to the cooling phase and a more prominent damping effect from secondary temperature budget terms when smaller scales are excluded and MHWs are merged into larger entities (Fig. 3a–e). As spatial scales increase, the proportion of ADV-dominated MHWs tends to decline, likely because eddy-driven, small-scale MHW features are either filtered out or merged into larger-scale events. Both factors can reduce the representation of eddy-driven MHWs as the spatial filter scale increases[40], thereby increasing the relative contribution of events dominated by mean flow advection. Such a shift in the underlying dynamics alters the composite temperature tendency budget evolution by emphasising heat transport associated with broader-scale, less transient circulation patterns.

Surface heat flux-dominated (Q-dominated) MHWs (Fig. 3f–j) are primarily driven by net positive downward surface heat flux, with smaller contributions from the other terms. As the event evolves, other components of the temperature tendency budget increasingly act to dampen the warming, accelerating the transition to decay even before the surface heat flux reverses to a net cooling effect in the later stages. Unlike ADV-dominated events, the composite mean of Q-dominated MHWs displays weaker dependence on the spatial scales in their temperature budget evolution (Fig. 3f–j), suggesting that the influence of air-sea heat flux on upper ocean warming is relatively insensitive to the spatial scale of the MHW.

Having verified that the temperature budget-based classification effectively distinguishes MHW objects driven by distinct local mechanisms throughout the event lifetime, we next examine the characteristics of these MHWs across varying spatial scales (Fig. 4). As the minimum spatial scale increases, smaller-scale features are naturally filtered out or merged together, resulting in larger MHW entities on average. Specifically, Q-dominated MHWs tend to exhibit larger spatial extents (area) compared to those driven by oceanic advection (Fig. 4a–e, Supplementary Fig. S3k-o). In contrast, ADV-dominated MHWs tend to persist longer as the spatial scale grows. For example, at the 0.5° spatial scale, the interquartile ranges are 8.0–29.0 days for Q-dominated MHWs and 10.0–45.8 days for ADV-dominated MHWs. Although less pronounced due to the logarithmic duration scales, this pattern remains discernible in Fig. 4a–e and Supplementary Fig. S3a–e. This feature reflects the suppression of mesoscale variability and highlights events maintained by persistent, larger scale mean currents. Metrics of Residual-dominated MHWs generally fall between those of MHWs driven by the two primary local drivers (Q and ADV). The intensity of MHW entities shows a weaker dependence on local drivers, as their probability distributions are not evidently separated in spatial scales from 0.5–2.0° (Supplementary Fig. S3f.-i). Only at the 2.5° scale do Q-dominated MHW entities tend to be stronger than those driven by oceanic advection (Supplementary Fig. S3j). Similar conditions are observed in MHW displacements (Supplementary Fig. S3p-t), where divergences between Q-dominated and ADV-dominated MHWs are only evident when considering MHW entities with spatial scales of 2.0°–2.5°.

The variability in MHW entities due to different local forcings is evident not only in their metrics but also in their temporal evolution. To examine this aspect, we first rescale the spatially integrated intensity time series of each MHW to a 0–1 range using min–max normalisation. We then align all events onto a common normalised temporal axis (0–1), where 0 represents the onset and 1 the termination, thereby standardising their duration while preserving their intrinsic temporal structure. This approach enables direct comparison across MHWs of differing lengths. We then composite these temporally normalised MHW intensity time series according to their dominant local drivers (Fig. 5a). For a composite across all MHWs in the Tasman Sea, we observe a generally symmetric temporal structure, with balanced growth and decay phases. However, temporal growth and decay asymmetries emerge when MHWs are classified by their associated forcing mechanisms. Compared to ADV-dominated MHW events, Q-dominated events reach their peak intensity later in the lifecycle ($t = 0.61 \pm 0.11$ vs. $t = 0.45 \pm 0.09$ for ADV-dominated events), characterised by slow intensification followed by rapid decay. This dichotomy is consistent with previous regional and event-based studies: Q-dominated events decay more abruptly because they are driven by the inherently transient nature of atmospheric forcing, whereas ADV-dominated events in the western boundary current region exhibit slower decay than growth, owing to the slow retreat of warm water transport favoured by strong ocean inertia[5,28,30,41–44]. Residual-dominated MHWs, which are not predominantly due to either ADV or Q forcings, resemble the canonical symmetric pattern but exhibit greater event-to-event variability, reflected in their larger standard deviations. This is likely a consequence of the smaller sample size of this category, resulting in a larger influence of outliers.

Considering MHWs as evolving entities rather than fixed-grid events enables us to examine the scale- and driver-dependent MHW temporal evolution within a spatiotemporal framework. To achieve this objective, we project the MHW entity at each time step along its track onto a standardised spatial domain—see Methods (Fig. 5b–e). From a composite perspective encompassing all events, MHWs in the Tasman Sea originate from a central warm core, and then expand uniformly outward, reach peak intensity around the midpoint of their lifespan, then gradually decay (Fig. 5b). The driver dependency found in the MHW temporal evolution (Fig. 5a) is also evident in its spatiotemporal evolution, as the normalised radial extension of the MHW warm core tends to be stronger during its growth phase than its decay phase in ADV-dominated MHWs relative to the Q-dominated ones.

Using the same approach as in Fig. 5, and detailed in the Methods, we examine the background weather conditions associated with the development of MHWs across different spatial scales, thus providing a dynamic and thermodynamic characterisation of MHW evolution driven by distinct local mechanisms. Figure 6 presents a composite of the spatiotemporal evolution of surface heat flux anomalies concurrent with the development of Q-dominated MHWs. MHW growth is accompanied by a centrally concentrated pattern of positive heat flux anomalies. These anomalous downward positive heat fluxes persist for approximately three-quarters of the MHW duration, before transitioning to negative (upward) anomalies after $t = 0.75$. This sustained Q anomaly prolongs the growth phase of the Q-dominated MHWs, consistent with the delayed peak in MHW intensity observed in these events (Fig. 5a, d). Notably, variations in the spatial scale over which MHWs are grouped together (rows in Fig. 6) do not significantly alter the structure of the associated heat flux anomalies throughout their development, except for increased spatial variability at larger spatial scales, likely associated with the smaller sample size of the larger events' group.

To further investigate the thermodynamic drivers, we analyse the co-evolution of decomposed surface heat flux anomalies over the full lifespan of the Q-dominated MHWs using the normalisation projection framework (Fig. 7a–d). The enhanced net downward surface heat flux observed during the early to middle stages of the MHWs is primarily attributed to a reduction in latent heat flux loss from the ocean to the atmosphere (i.e., positive downward latent heat flux anomalies; Fig. 7a). Shortwave radiation contributes a smaller but still noticeable proportion to net heat flux changes during the lifespan of the MHWs, resulting from clearer skies

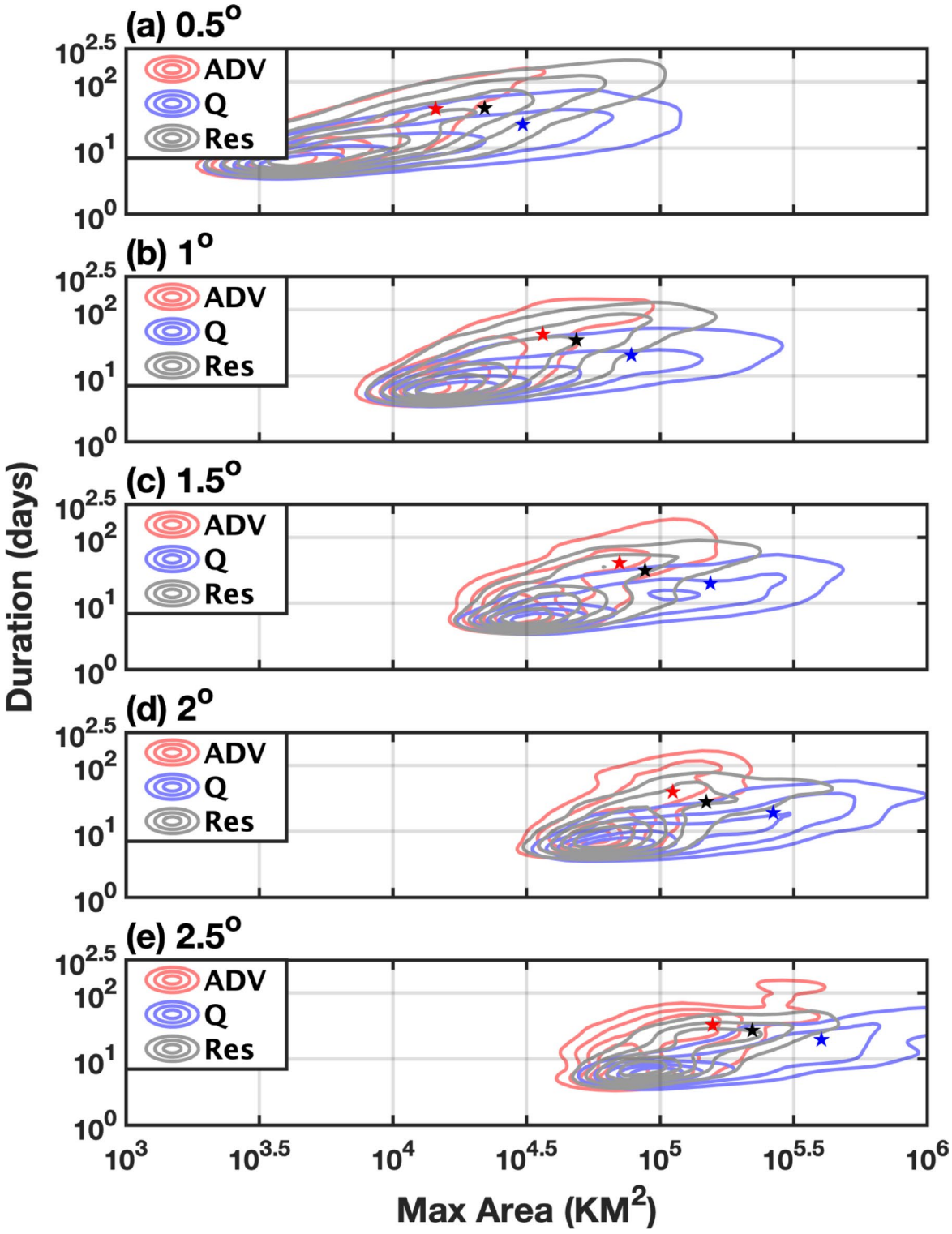

Fig. 4. Joint probability distribution of MHW duration and maximum area. (**a**–**e**) Kernel density estimates of MHW occurrences across spatial smoothing scales from 0.5° to 2.5°. Distributions are categorised by dominant local drivers: surface heat flux (Q), horizontal advection (ADV), and residual processes (i.e. neither Q nor ADV are dominant). Contours denote probability density, and pentagrams indicate the mean duration and maximum area for each driver category. Kernel density estimation was performed on the log-transformed metrics with a bandwidth of 0.1.

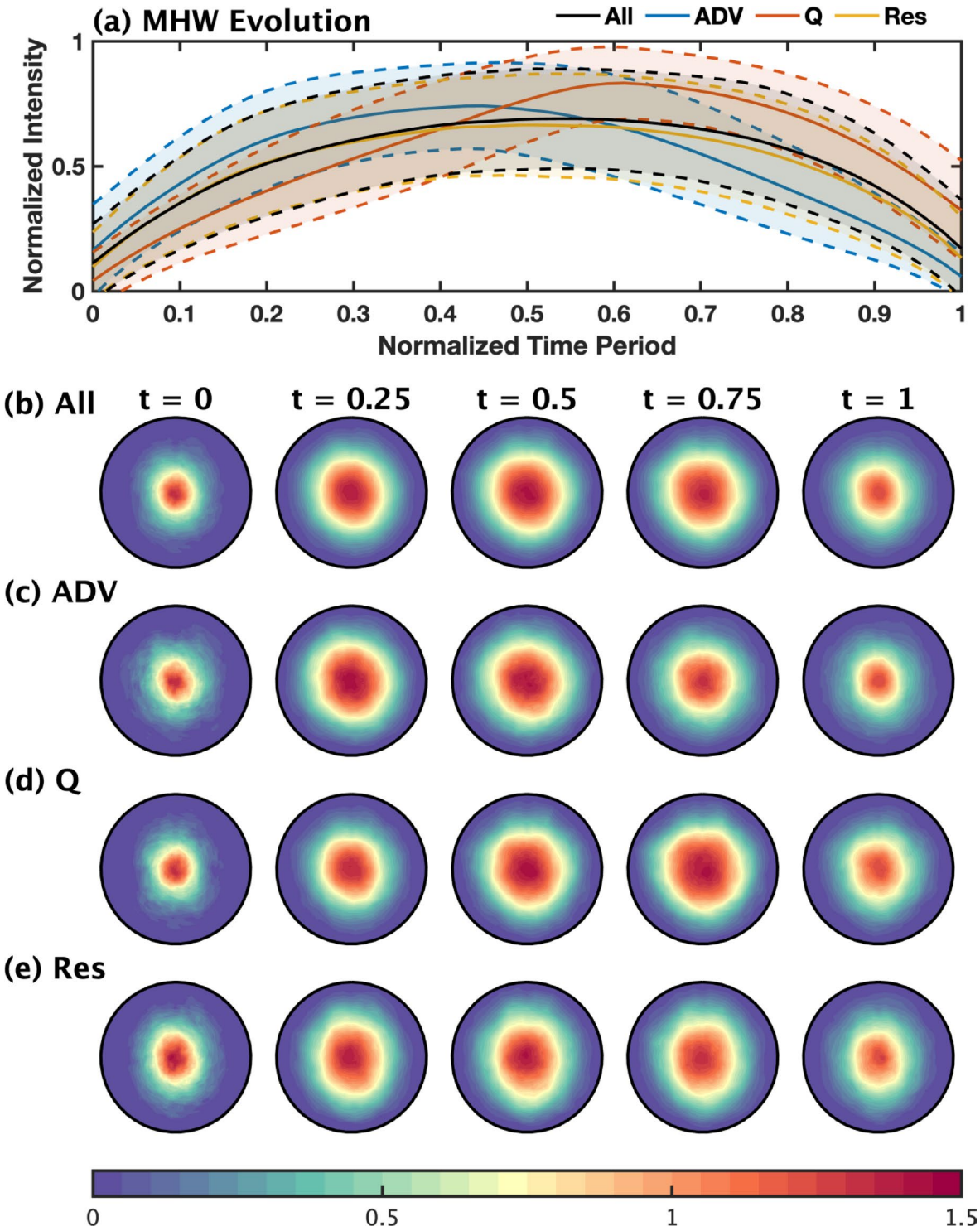

Fig. 5. MHW evolution conditioned on dominant local drivers for a spatial filter scale of 0.5°. (**a**) Temporal evolution of normalised MHW cumulative intensity, composited over all events and subsets driven by distinct local drivers: oceanic advection (ADV), air–sea heat flux (Q), and residual processes (Res). Shading denotes interquartile range (25th–75th) as a measure of confidence. (**b**–**e**) Spatiotemporal evolution of MHW intensity (expressed as sea surface temperature anomaly, °C), composited for (**b**) all MHWs and for events primarily driven by (**c**) oceanic advection, (**d**) air–sea heat flux, and (**e**) residual processes, and projected onto a unit circle to enable morphological comparison (see Method). Each column represents a phase of the MHW life cycle along its trajectory: onset (t = 0), early (t = 0.25), middle (t = 0.5), late (t = 0.75), and termination (t = 1) stages.

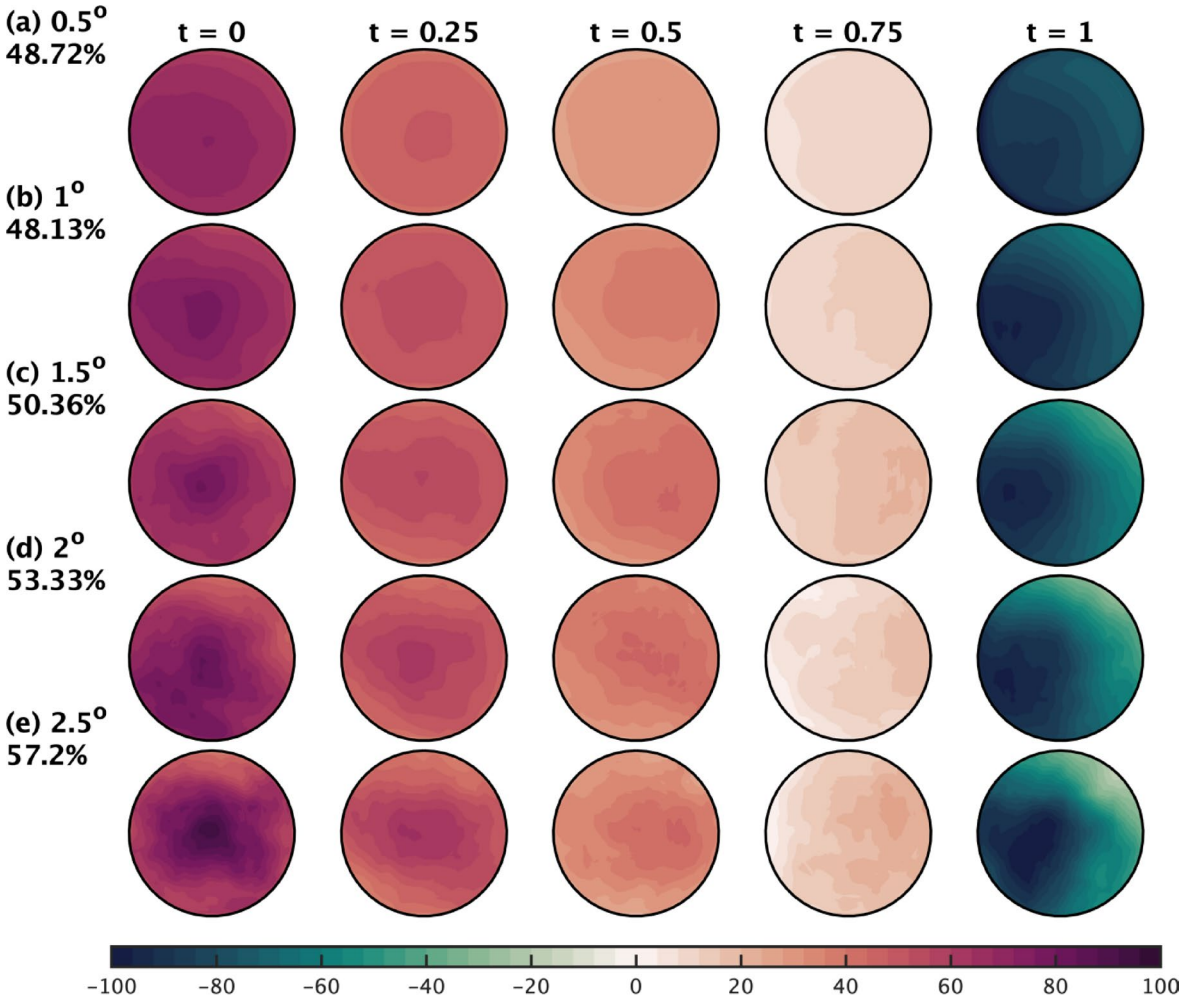

Fig. 6. Spatiotemporal evolution of net surface heat flux anomalies for Q-dominated MHWs. (**a**–**e**) Composited anomaly patterns of net surface heat flux anomalies (W m^{-2}; sum of latent, sensible, shortwave, and longwave components) at varying spatial filter scales (0.5–2.5°). Columns represent normalised phases of the MHW life cycle from onset (t = 0) to termination (t = 1). All panels are composited across Q-dominated MHW events and projected onto a unit circle to enable morphological comparison using the same method for Fig. 5b–e. Statistical significance estimated using a t-test exceeds 95% confidence across nearly all the area of each panel (stippling omitted for clarity). Percentages indicate the fraction of all MHW entities classified as Q-dominated at each spatial scale.

during early MHW phases (Fig. 7e, t = 0–0.5). In contrast, contributions from sensible heat flux and longwave radiation are comparatively minor (Fig. 7b, d). Wind stress is persistently suppressed throughout the onset and subsequent lifespan of the MHWs (Fig. 7g, t = 0–0.75), which reduces surface latent heat loss and likely weakens vertical mixing. This leads to consistent shoaling of the mixed-layer depth during the lifespan of MHWs (Fig. 7f), further enhancing upper ocean warming due to atmospheric forcing, a series of processes that led to the exceptional 2023 North Atlantic warming[12]. This comprehensive analysis refines and extends the Q-dominated MHW framework originally identified in previous studies[2], emphasising the continuous and critical influence of air-sea heat fluxes throughout the entire MHW lifecycle, rather than interpreting their role as an averaged effect during MHW occurrence.

Compared to Q-dominated MHWs, the local drivers of ADV-dominated MHWs display quite different spatial structures. Figure 8 illustrates the spatiotemporal evolution of oceanic advective heat flux convergence composited during the lifespan of ADV-dominated MHWs. For MHWs detected at fine spatial scales (considered here at scales of 0.5° and 1°), the anomalous temperature tendency due to advection is enhanced during the early phase of the composited MHW and then suppressed, contributing to the decay of the MHW in its later phase, and consistent with the results found in the temperature tendency budget analysis. It is worth noting that the spatial pattern of mixed-layer oceanic advection becomes increasingly noisy and loses statistical significance as MHWs are grouped together over larger spatial scales, a feature likely arising from the aggregation of mesoscale eddy structures, which merge to form larger-scale MHW events, and a sample size which is too small to average out this statistical noise. This result is also consistent with previous findings indicating the shifting local driver of a MHW as its spatial scale increases, from mesoscale eddy-driven to large-scale mean flow driven-

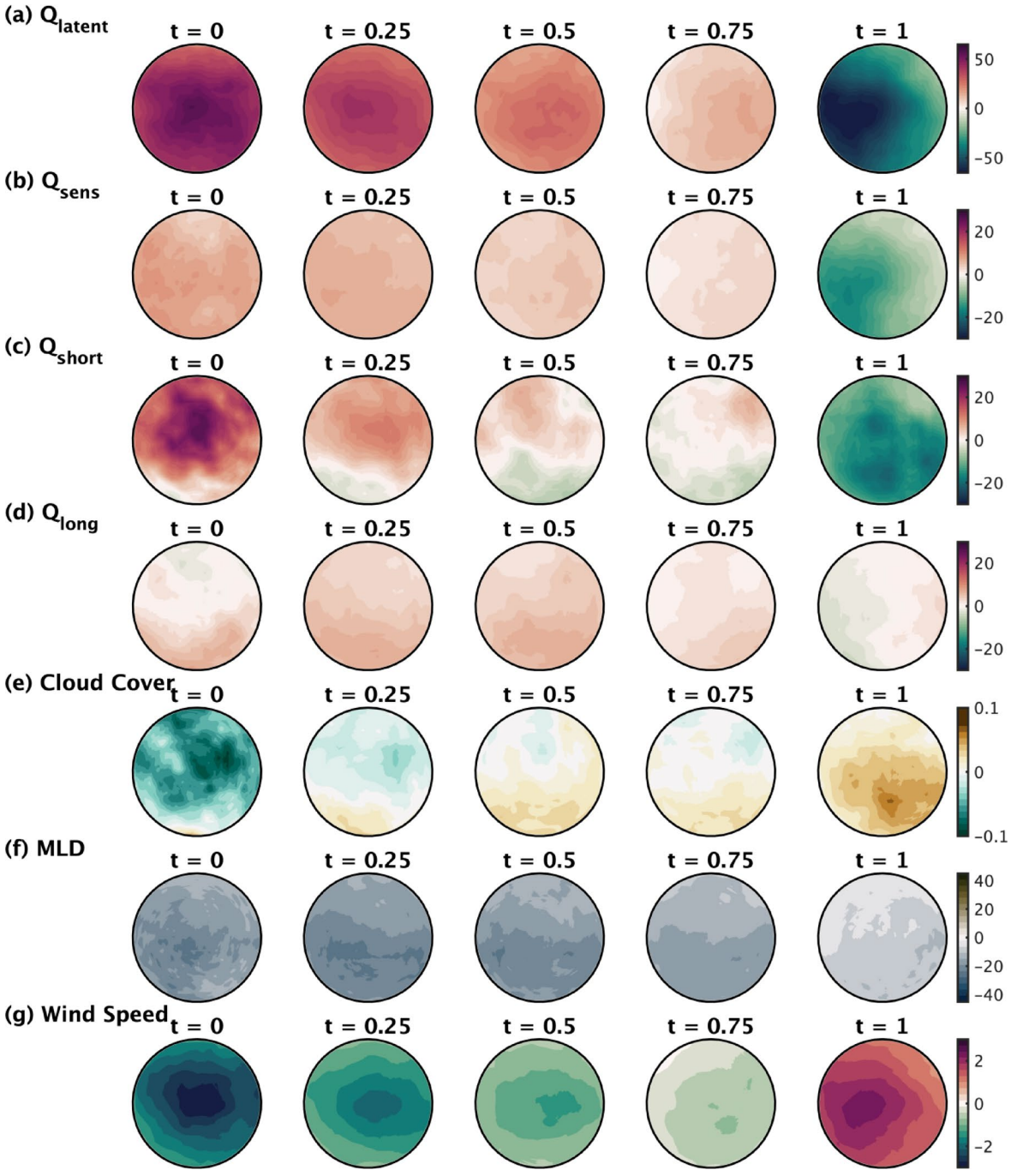

Fig. 7. Spatiotemporal evolution of heat flux components and background conditions during Q-dominated MHWs. Composited anomaly patterns of (**a**) latent heat flux, (**b**) sensible heat flux, (**c**) shortwave radiative flux, and (**d**) longwave radiative flux (all W m^{-2}), alongside background atmospheric and oceanic states: (**e**) cloud cover, (**f**) mixed layer depth (**m**), and (**g**) wind speed (m s^{-1}). Columns represent normalized phases of the MHW life cycle from onset (t = 0) to termination (t = 1). All panels are composited across Q-dominated MHW events and projected onto a unit circle to enable composite analysis using the same method as in Fig. 5b–e. Results shown correspond to the 2.5° spatial scale. Values are statistically significant at 95% confidence (estimated using a t-test) in most of each panel.

events at roughly a 1–1.5° scale[40] (Fig. 8a, b), which is proportional to the Rossby radius of deformation in the midlatitudes. Another notable feature is the pronounced asymmetry in the spatial distribution of mixed-layer advection within the MHW domain: unlike the air–sea heat fluxes with a warm core slightly concentrated near the MHW centre during Q-dominated events (Fig. 6), the maximum warming tendency associated with oceanic advection is consistently located in the southwestern portion of the MHW domain (t = 0–0.5 in Fig. 8a). This spatial displacement likely reflects a southward heat transport by advection (e.g., southward-propagating East

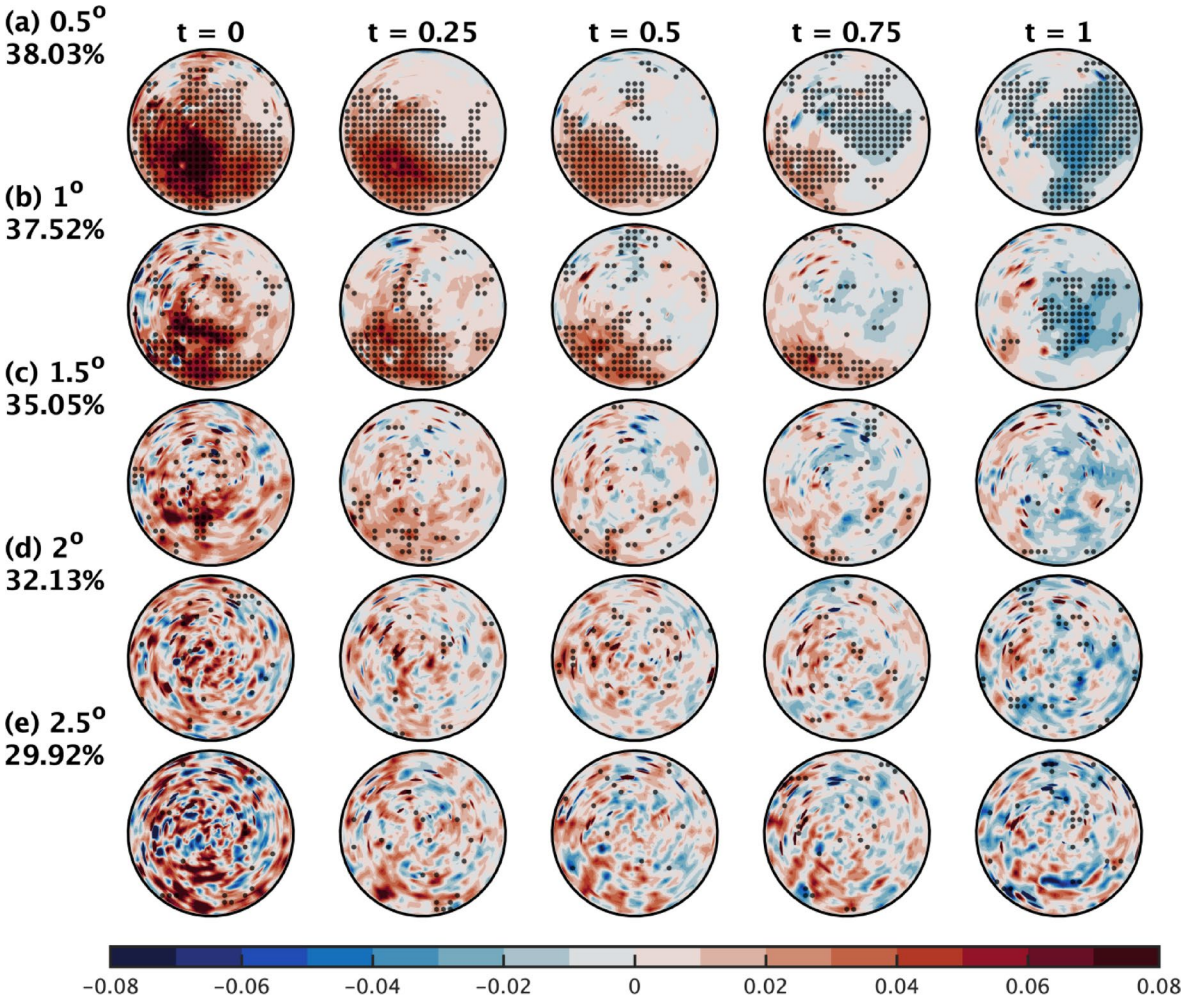

Fig. 8. Spatiotemporal evolution of oceanic advection anomalies during ADV-dominated MHWs. (**a**–**e**) Composited anomaly patterns of mixed layer temperature tendency due to oceanic advective heat flux convergence (°C day^{-1}) at varying spatial filter scales (0.5–2.5°). Columns represent normalised phases of the MHW life cycle from onset (t = 0) to termination (t = 1). Dots indicate 95% statistical significance, determined through a t-test. All panels are composited across ADV-dominated MHW events and projected onto a unit circle to enable composite analysis using the same method as in Fig. 5b–e. Percentages indicate the fraction of all MHW entities classified as ADV-dominated at each spatial scale.

Australian Current Extension eddies), leading to advective heating in the south and corresponding cooling in the north as the MHW nears termination. The advective heating term is displaced from the sea surface temperature (SST) anomaly peak in Fig. 5c because it is proportional to the upstream SST gradient (Eq. 1 in Methods), so it is maximum on the downstream flank of the SST anomaly peak. These results are consistent with some recent studies on MHW local drivers under different spatial resolutions. For example, using a coarse-resolution model, ref[38] found that atmospheric heat fluxes are the main driver for the onset and decay of MHWs globally, while separate studies using eddy-resolving models or ocean state estimates that can close the heat budget exactly[45] found that oceanic advection could be either comparable or more important[37,46]. Ref[40] further suggests a transitioning scale of MHW drivers from ocean-dominant to atmosphere-dominant as the spatial resolution becomes coarser. Here, the larger spatial smoothing scale serves as a proxy for coarser spatial resolution, which reduces the role of narrow ocean currents and/or mesoscale eddies, as highlighted by the reduction in MHW occurrences in the EAC and its Extension—that is, a reduced percentage of ADV-dominated MHWs, and less evident kinematic evolution patterns of the advection anomalies.

Lastly, we characterise the vertical structure of MHW events associated with the two key drivers (Q-dominated and ADV-dominated) by compositing the spatially integrated MHW severity index across entities dominated by each driver, following the approach described in the Methods. The Q-dominated and ADV-dominated MHWs have clear differences in their depth extent (Fig. 9). In our Tasman Sea case study region, subsurface warming in Q-dominated MHWs is largely confined to the upper ~ 30 m (Fig. 9a–d), while ADV-dominated MHWs exhibit significant warming extending to at least 300 m depth (Fig. 9f–j). This is attributed to the local dynamics. Surface heat fluxes tend to increase stratification and lead to surface-intensified events[2]. Advection, which is especially pronounced in the western boundary EAC and its Extension[47,48], as well as in the Tasman Front and the East

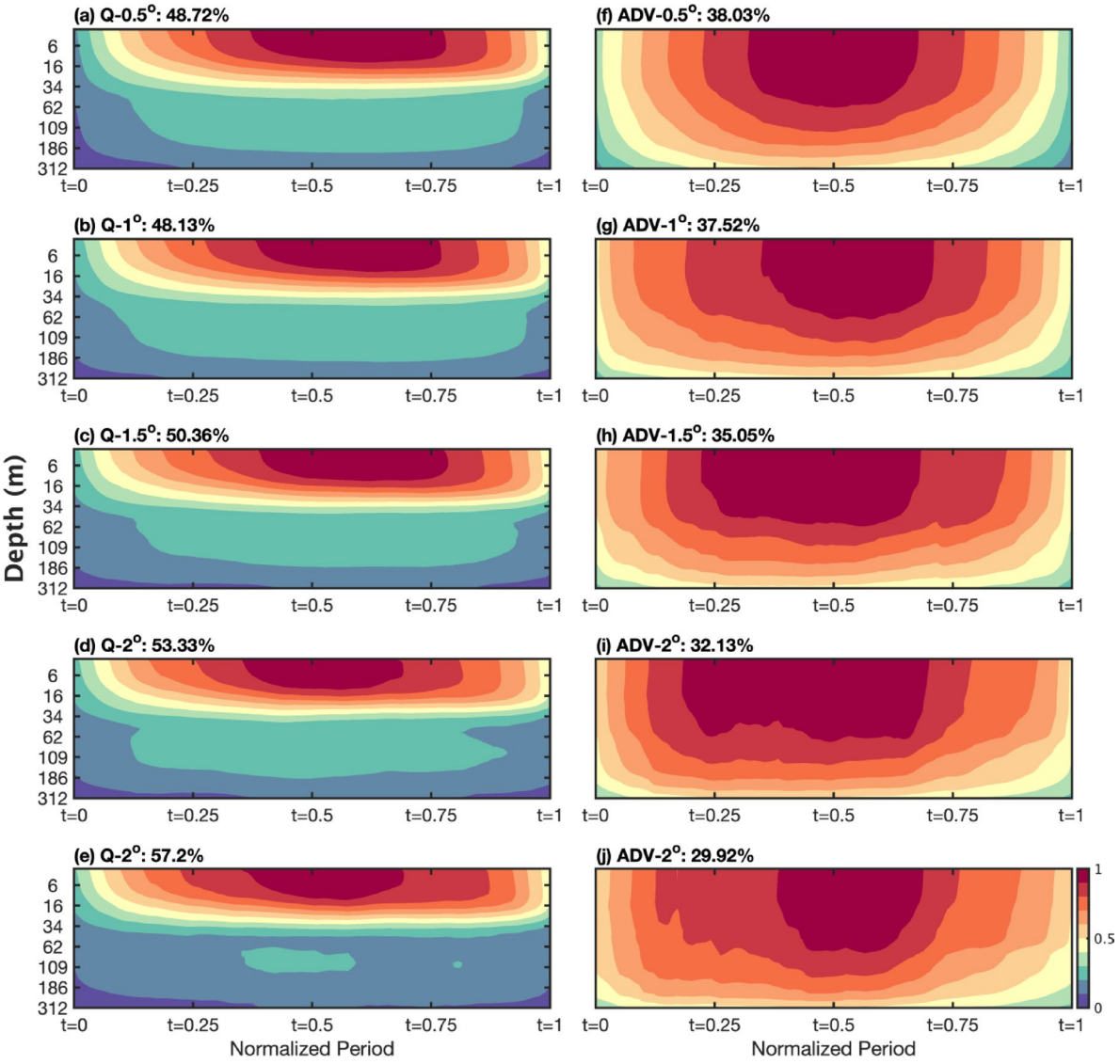

Fig. 9. Vertical structure evolution of Tasman Sea MHW-composites through their lifespans for different spatial scales. Colours here indicate spatially integrated MHW severity index scaled by its maximum (0–1). Each column indicates results composited from either (**a**–**e**) Q- or (**f**–**j**) ADV-dominated MHWs. Note that vertical scale is nonlinear to highlight the upper ocean. Proportions of corresponding MHW entities are labelled in the title of each panel. Total numbers of MHW entities for spatial scales 0.5–2.5° are 9,920, 3,577, 1,646, 856, and 528 events, respectively.

Auckland Current[49,50], extends deeper into the water column with a less stratified upper ocean[30,51,52], and is attributed to anomalous warm water transport such as by eddies[29,37,39]. This contrast tends to be persistent across varying spatial scales. The asymmetry in surface MHW intensity evolution (Fig. 5a) persists in the subsurface structure, as evidenced by the largest subsurface warm anomalies emerging during the later (early) phases of Q- (ADV-) dominated MHWs across many spatial scales.

Discussion

While MHWs have been extensively studied, our understanding of their dynamics and predictability as moving objects has been limited. This is because most existing methods used for MHW detection and analysis rely heavily on pointwise statistical approaches, primarily applied within Eulerian frameworks[1,2]. While computationally efficient, analyses of MHWs within fixed regions or boxes, including heat (or temperature tendency) budgets to determine their local drivers, often fail to capture the true nature of MHWs, which may be more properly described as evolving objects in both space and time.

Taking advantage of previously developed tracking approaches[23–27,53,54], this study presents a mechanistic characterisation of MHWs within a semi-Lagrangian framework that treats MHWs as coherent entities evolving in space and time. Furthermore, by applying a scaling method that normalises the spatiotemporal variability of MHWs into a standardised domain, our framework enables a composite analysis of these mobile events and

their potential drivers throughout their entire lifespans, while accounting for spatial dependencies. By analysing MHWs as evolving objects—from genesis to decay—the application of the semi-Lagrangian approach provides a novel perspective on the physical and (thermo-)dynamical processes that govern MHWs. This approach has allowed us to examine different aspects of these MHW events, while accounting for their scale—an important factor for impact studies, and for achieving clearer links to the key MHW drivers. This framework also advances current understanding of MHW evolution in space and time beyond statistical characterisations, offering insights into their dynamic and thermodynamic mechanisms, with the potential of informing prediction studies.

A key strength of the semi-Lagrangian approach is its ability to maintain spatiotemporal coherence[23,24,26,27]. This is achieved by identifying MHWs as spatially connected anomalies—as objects, or entities—evolution can be tracked in space and time. Such coherence enables a comprehensive examination of MHW evolution from onset to end. This is critical not only to understand MHW kinematics of growth and decay, but also their dynamics through the analysis of different temperature tendency (or heat) budget terms and associated local drivers within the moving space–time frame of reference of these objects. The ability to characterise the connection of the evolving MHW objects with their drivers can be expected to enhance our understanding of their predictability, and aid forecasting efforts. The approach is also likely to inform studies aimed at elucidating the links between MHWs and other ocean extremes, like ocean hypoxia[55,56] and and acidification[57].

Using the Tasman Sea as a case study—where both ADV- and Q-dominated MHWs are clearly observed—, our temperature budget analysis extends previous diagnostics of local MHW drivers from fixed grid cells to dynamically evolving spatiotemporal entities. Previous heat (or temperature) budget analyses have typically been presented either as spatially averaged time series over the lifespan of individual MHW events[31,41,43,58,59], or as composite maps in which each grid cell represents heat budget terms averaged across all MHW occurrences or stratified by growth and decay phases[30,37–40,45,46]. The former approach is well suited for characterising the temporal evolution of local drivers during specific MHW events but becomes less practical when applied at the grid-cell level. The latter approach can identify dominant local drivers across MHWs, yet restricting the analysis to growth and decay phases is often insufficient to capture the full MHW evolution, as many events do not exhibit well-defined growth–decay characteristics[60]. By integrating the tracking and normalisation framework developed here with grid-cell-based local temperature tendency budgets, we are able to express the composite evolution of local drivers across both temporal (Fig. 5a) and spatiotemporal (Figs. 5, 6, 7, 8) dimensions, while accounting for variations in the shape, size, and duration of MHW entities. This framework substantially expands the scope of local MHW driver analyses and is particularly advantageous when applied to online-calculated heat budget model outputs or more comprehensive anomalous water-mass budget diagnostics.

Although oceanic advection plays a dominant role in the development of MHWs identified at high-resolution grid cells in the Tasman Sea from a Eulerian perspective[37,46], a smaller fraction of tracked MHW entities is dominated by oceanic advection relative to other local drivers (e.g. only 38.03% of tracked MHW entities are identified as ADV-dominated at the 0.5° spatial scale). This discrepancy likely arises because grid-cell-scale MHW occurrences are more strongly influenced by eddy-scale processes[37,40,46], which are largely averaged out when events are analysed as spatially connected objects. The contrast between driver attribution from Eulerian and semi-Lagrangian perspectives further highlights the need to examine the temporal evolution of local drivers within the lifespan of MHWs—particularly for extreme events—as reliance on composite maps alone can obscure the temporal concurrence of MHWs across adjacent grid cells.

Despite its advantages, the semi-Lagrangian approach is not without challenges. One such challenge is that the temperature budget analysis applied here remains incomplete from a moving-object perspective, as it does not explicitly quantify boundary-change effects of MHW entities in the anomalous fields. This is because the anomalous temperature tendency budget terms are calculated at the grid-cell level and then assigned to corresponding MHW entities, rather than being diagnosed for individually tracked MHW objects as in ref[61] (see Methods). Additionally, assigning each MHW entity that demonstrates spatiotemporal variability to a unique local driver may be insufficient to characterise the full evolution of a MHW entity's heat transport lifecycle. This will make the spatial heat transport pattern diverge from the MHW spatial patterns, especially for energetically moving events, like the ADV-dominated events here. This may be part of the reason for the non-centred located heat transport shown in mid-to-late phases of ADV-dominated MHW entities (Fig. 8). A conceivable alternative approach would be to construct heat budget time series of all MHW entities, normalise them, and apply cluster analysis to extract the dominant driver patterns. However, this would overcomplicate the narrative and deviate from our primary objective here: that is, summarising the kinematic and dynamic features of MHWs to their specific drivers as undertaken in ref[2]. Even so, these considerations still point to potential future directions on this topic.

A major motivation for advancing methods to track the evolution of MHWs and to be able to predict them is to better understand their likely socioeconomic impacts[62]. For marine species that can move, e.g., pelagic or demersal fishes that swim, the semi-Lagrangian characterisation of the dynamics and potential predictability is likely to be highly advantageous, as it provides much greater understanding of the scale of these events in space and time, and how they can affect species distributions. For benthic marine organisms, such as foundational species including corals, kelps, and seagrasses that are fixed to the seafloor and potentially vulnerable to MHWs[14], the semi-Lagrangian approach to MHWs also offers value, as it enables assessment of how the passage and timing of a moving MHW influences marine ecosystems at specific locations, such as within defined marine ecoregions.

The findings of this study highlight several promising directions for future research. First, the development of hybrid approaches that leverage the strengths of both Eulerian and semi-Lagrangian perspectives could provide a more nuanced understanding of MHWs. Such approaches could incorporate dynamic tracking for large-scale analysis while preserving small-scale variability for impact studies. Second, there is a need for improved heat (or temperature tendency) budget diagnostics that account for the boundary changing effect of evolving

MHW entities defined using anomalous fields. Developing methods that integrate spatiotemporal dynamics into temperature budget analysis could enhance our ability to attribute temperature changes to specific drivers, particularly in regions with complex oceanic processes. In addition, connecting the evolving nature of MHWs to large-scale climate drivers would be very useful to anticipate their onset and subsequent propagation pathways. Finally, the application of semi-Lagrangian methods to interdisciplinary research offers substantial possibilities. By aligning MHW studies with research on other spatiotemporally evolving phenomena, such as atmospheric heatwaves, tropical cyclones, atmospheric rivers or biogeochemical extremes in the ocean, it may be possible to investigate the interactions between these different societal and ecological stressors. This interdisciplinary approach could provide new insights into the compounding influences and impacts of various phenomena.

This study demonstrates that the afore-described application of a semi-Lagrangian framework can be beneficial to mechanistically advance our understanding of MHWs. By treating MHWs as coherent, evolving entities in space and time, analysing temperature budgets in a moving frame of reference, and capturing their dynamic evolution within a normalised coordinate system, this approach provides a physically grounded characterisation of MHW development and decay from both dynamic and thermodynamic perspectives. Despite some remaining challenges—particularly regarding computational demands and the complexity of temperature budget diagnostics—the benefits of this method are evident. As future research continues to refine and extend this framework, the semi-Lagrangian approach holds strong potential to become a foundational tool for studying MHW dynamics and their ecological and climatic impacts in a warming world.

Methods

Atmosphere and ocean data

The variables used to characterise the evolution of atmospheric conditions during marine heatwave (MHW) lifecycles include sea level pressure, sensible and latent (convective) heat fluxes, longwave and shortwave (radiative) heat fluxes, cloud cover, and wind speed. In this study, these variables were obtained from the Japanese 55-year Reanalysis (JRA-55)[63] for the period 1987–2018. JRA-55 is a second-generation global atmospheric reanalysis developed by the Japan Meteorological Agency, incorporating advanced data assimilation techniques and improved model physics relative to earlier reanalyses. Its reliability in representing large-scale atmospheric circulation and surface fluxes has been demonstrated across various regions and applications[63,64], and it has been utilised in numerous climate and extreme event studies, including those involving ocean–atmosphere interactions and extremes such as MHWs. To maintain consistency with the daily resolution of sea surface temperature data used for MHW identification, the original higher-frequency JRA-55 data were averaged to a daily timescale.

Sea surface temperature (SST) (typically used to detect MHWs), subsurface ocean temperature, and mixed layer depth (MLD) were extracted from the eddy-resolving (0.1°) simulation of the Australian Community Climate and Earth System Simulator Ocean Model Version 2 (ACCESS-OM2-01)[65,66], forced by prescribed fields from the Japanese 55-year atmospheric reanalysis for driving the ocean, version 1.4 (JRA-55-do v1.4), which is based on JRA55 but includes many adjustments to reduce model drift[67]. We use outputs from the first forcing cycle, which starts from World Ocean Atlas 2013 initial conditions and covers the spatial domain of the Tasman Sea (Fig. 1). Outputs include daily oceanic properties from 1958–2018 for the surface layer and from 1987–2018 for the subsurface (75 vertical levels), respectively. These outputs have been used and evaluated in other previous studies, including those examining global and Australian region MHWs[68–70], and confirm the model's ability to simulate global and regional-scale patterns well, while providing mesoscale detail that is typically missing in large-scale observational datasets[71], such as the widely used 0.25° optimally interpolated SST observations from the US National Oceanic and Atmospheric Administration (OISST)[72,73]. Being a free-running (not data-assimilating) model, it remains dynamically balanced.

Detection of MHWs using fixed-grid and semi-Lagrangian approaches

The detection of MHW entities begins with the typical Eulerian identification of MHW occurrences at each location. Here, we follow the definition proposed by ref[1], which determines MHW events based on SSTs exceeding the seasonally varying 90th percentile threshold for a minimum duration of 5 days. The application of this definition results in a binary map at each location and time step (the daily MHW snapshots[27]), where true (1) indicates MHW presence and false (0) corresponds to MHW absence. Direct application of the MHW detection criteria outlined by ref[1] often yields spatially fragmented patterns, characterised by isolated MHWs at individual grid points that lack spatial coherence. This fragmentation is attributed to the pointwise nature of the detection method, which is sensitive to both the spatial resolution of the data, and the use of the 90th percentile as a MHW detection threshold, without consideration of the underlying physical dynamics.

The Eulerian detection method may occasionally yield isolated MHW locations or small regions within larger-scale MHWs that do not strictly exceed the defined threshold. Such occurrences could arise from small-scale oceanic processes, localised variability, or data inaccuracies or uncertainties. Given the assumption that extensive MHWs are driven primarily by physical mechanisms operating over large spatial scales[28], it is reasonable to remove these smaller-scale features to preserve the coherent spatial structure of the event. Therefore, implementing an appropriate smoothing procedure is justified to accurately represent the overall shape and evolution of MHWs and thus retain tracked MHWs in certain spatial scales. Previous studies have used either the K-Nearest Neighbour (KNN) method[27] or image processing (IP) techniques[26] to describe MHWs of a certain spatial extent and eliminate isolated grid points. Ref[27] used a KNN classifier to smooth daily MHW snapshots, trained by the raw MHW presences and absences, leading to two-dimensional (2D) MHW objects as smooth shapes suitable for temporal tracking. Conversely, ref[26] processed the raw MHW binary maps using morphological "opening" and "closing". The morphological opening, consisting of consecutive dilation and erosion processes, aims to remove isolated features while retaining the shape of the large MHW objects.

In contrast, the morphological closing, which is the reverse process of opening, has been used to fill isolated "holes", thereby preserving the spatial coherence of the large MHW objects. By comparing outputs from the two methods under different smoothing scales using a MHW snapshot around Australia, we have found that the KNN method tends to provide smoother MHW objects while retaining their shapes and sizes (Supplementary Fig. S4). Conversely, the IP method applied by ref[26] can introduce some unrealistic information as the smoothing scale increases. Hence, here we use the KNN method to smooth the raw MHW binary maps.

It should be noted that the spatial smoothing applied here does not always eliminate isolated MHW occurrences; in some cases, it can introduce artificial MHW signals through the "filling holes" processes during the regulation of MHW shapes. To assess how considerable this effect is, we calculate the False Alarm Rate (FAR) of processed MHW occurrences (Supplementary Fig. S5). The FAR represents the proportion of MHW absences that are labelled as MHW presences after processing by the KNN method, providing a metric to quantify the disagreement between raw and processed MHW signals. When applying spatial smoothing at scales between 0.5° and 2.5°, the spatial patterns of the FAR are relatively uniform over the Tasman Sea, with a mean value of 0.7% and a maximum of 5%. This indicates that the tendency of spatial smoothing to introduce new MHW occurrences is minimal compared to its effects of removing existing MHW signals, particularly that are isolated at smaller spatial scales. This finding further confirms the primary role of smoothing here in reducing isolated MHW occurrences and connecting discrete MHW features.

The framework of ref[27] involves tracking 2D MHW objects formed by connected grid cells that exceed the MHW threshold within each MHW binary map. This method achieves a spatially coherent representation of MHW spatiotemporal evolution, similar to tracking oceanic eddies and tropical cyclones. In this framework, MHW objects from consecutive time steps are considered part of the same "track" if the area of overlap exceeds 50%. Throughout the tracking process, three different scenarios are considered, i.e., general transitions, splitting events, and merging events. It is important to note that when a MHW splits, provided the overlap criteria are met, each part is considered part of the original MHW. On the other hand, when two or more distinct MHW objects merge, the process is handled sequentially. At each time step, overlapping regions are assigned to the MHW track with the closest proximity to those regions. This procedure is iteratively applied until no overlapping regions remain. More complete details of the tracking process are provided by ref[27].

Instead of tracking 2D MHW objects to form MHW entities, some studies directly identify spatiotemporally connected MHW entities from 3D (latitude, longitude, time) binary MHW data[23–25]. Methods under this framework can result in spatiotemporally connected but spatially incoherent MHWs, often referred to as MHW systems or macro events. By comparing the output of this method with previously identified MHW objects in a case study region around southern Australia—including the Tasman Sea global warming hotspot[43]—we found that this method tends to classify certain spatially disconnected MHWs as a single, large-scale MHW system, since these events are temporally linked by intermediate discrete MHW occurrences (Supplementary Fig. S6). For instance, the spatiotemporal MHW resembling the 2015/16 Tasman Sea MHW is represented differently by the spatially coherent[27] (Figure S6a-d) and incoherent methods[24] (Supplementary Fig. S6e-h). Using the method proposed by ref[27], we identify a single, coherent structure evolving continuously over time. In contrast, the approach of ref[24] initially reveals spatially disconnected structures, which are subsequently classified as part of the same entity once they evolve into overlapping features. The spatially incoherent features of MHWs from the ref[24] method may complicate the identification of their drivers, as MHWs that remain spatially disconnected even after smoothing are less likely to be driven by the same forcings. However, during the merging process, if an overlapped MHW object is substantially smaller than the adjacent larger ones, it may be directly merged into them without undergoing the iterative procedure described in the Methods. As a result, the early development phases of these smaller MHW features may be overlooked when analysing the lifecycle of the larger events. For example, the origin of the western portion of the MHW on 27 December 2015 (Supplementary Fig. S6h) can be traced back to the preconditioning processes associated with a distinct, initially isolated western MHW (Supplementary Fig. S6e–g). Such mechanisms may not be captured by the diagnostics of spatially coherent MHWs presented in Supplementary Fig. S6a–d. Nevertheless, for assessing the overall structure and diagnosing the dominant mechanisms, the spatial coherence-based method remains preferable, as it effectively filters out contributions from spatially disconnected MHW features.

We thus apply the method of ref[27] to track MHW entities in the Tasman Sea from 1987 to 2018, using the fixed-grid MHW detected from ACCESS-OM2 SST data and processed at smoothing scales ranging from 0.5° to 2.5° in 0.5° increments. This yields five MHW entity datasets containing 9,920, 3,577, 1,646, 856, and 528 events, of which 14.9%, 13.7%, 13.0%, 12.7%, and 12.1%, respectively, involve splitting or merging processes during their lifespans. As the smoothing scale increases, the number of tracked MHW entities decreases, and the events exhibit increasingly coherent spatial structures. The proportion of splitting and merging cases also declines with larger smoothing scales, as finer-scale features are progressively suppressed and MHW objects are more consistently retained. Similar to fixed-grid MHWs, a suite of metrics can be defined for tracked MHWs, including duration, intensity, area, and spatial displacement, characterised in terms of time series (Supplementary Table S2), as well as their mean, maximum, and cumulative values.

Along-track temperature budget analysis to determine local MHW drivers

To identify the dominant local causal processes of MHWs, we apply a mixed-layer temperature tendency budget analysis (Eq. 1) to examine the local drivers of MHW entities (averaged across the interior pixels) along their tracks[74,75]:

$$\frac{\partial T}{\partial t} = -\boldsymbol{u}.\nabla T + \frac{Q - Q_h}{c_p \rho h} + residual \tag{1}$$

where $\frac{\partial T}{\partial t}$ is the mixed-layer temperature tendency, $-u.\nabla T$ is the temperature change due to horizontal advection within the mixed layer, and $\frac{Q-Q_h}{c_p \rho h}$ is the mixed layer temperature change contribution due to the surface heat flux. Here, u is the depth-averaged horizontal velocity within the mixed layer, Q is the net heat flux across the ocean surface and Q_h is the attenuated shortwave heat flux that escapes out of the base of the mixed layer [76], c_p is the specific heat capacity of seawater, ρ is the density of seawater, and h is the depth of the mixed layer. The residual term, defined as the difference between the left-hand side (LHS) and right-hand side (RHS) of Eq. 1, includes contributions from exchanges with the subsurface ocean (entrainment through the base of the mixed layer and turbulent mixing), the horizontal and vertical diffusion, and the numerical errors due to offline calculations.

In the present analysis, we calculate the four terms of Eq. 1 at each grid point within the ocean mixed layer offline, using outputs from the ACCESS-OM2, and further calculate their anomalies by removing their local seasonally varying climatology during 1987–2018. For each MHW pixel (i.e., each grid cell within a MHW entity), the dominant causal process is defined as the temperature-budget term on the right-hand side (RHS) of the equation that has the largest magnitude, shares the sign of the temperature tendency, and exceeds the sum of the other two RHS terms. By doing so, each MHW pixel (spatial grid at each time step) can be identified as either heat flux (Q) dominated, advection (ADV) dominated, or Residual dominated (that is, dominated by a combination of the remaining terms rather than either advection or surface heat flux as the dominant term). It is worth noting that Residual-dominated MHWs also include cases lacking a locally identifiable driver, which does not meet the two criteria outlined above. Supplementary Figs. S7-S9 illustrate the proportion of MHW occurrences dominated by different local drivers (ADV, Q, and Residuals) based on both raw and spatially smoothed data. In the EAC and its Extension regions, ADV MHWs dominate (Supplementary Fig. S7). However, as the spatial filter scale increases, a greater proportion of advection-driven MHWs are filtered out compared to other types of MHWs across most of the Tasman Sea. The application of spatial smoothing reduces the relative contribution of ADV-driven MHWs, revealing a relatively stronger contribution from other local drivers (Supplementary Fig. S8). Notably, Residual-dominated MHWs account for a smaller fraction of events than the other two categories and exhibit a more irregular spatial distribution, with hotspots primarily concentrated in coastal regions (Supplementary Fig. S9), underscoring the dominant influence of the two principal local drivers (ADV and Q) across the entire region.

Consequently, the dominant driver of each MHW entity along its trajectory is identified as the temperature tendency budget term that accounts for more than 50% of the pixels within the object's spatiotemporally evolving contiguous boundary over its lifetime. Notably, we use the proportion of pixels—rather than the cumulative temperature tendency contributed by each temperature budget term—to avoid potential biases arising from extreme values in isolated grid cells.

Note that the net heat flux (Q) and its components are calculated from JRA55 reanalysis rather than JRA55-do, which ACCESS-OM2-01 uses to calculate the forcing fluxes. This choice is necessary because the estimation of Q requires both upward and downward shortwave and longwave radiation, but these were not saved separately from the model run and JRA55-do provides only the downward components. As a result, the atmospheric conditions represented in the temperature budget differ slightly from those driving ACCESS-OM2-01, due to both the differences between JRA55 and JRA55-do, and because the latent, sensible and upward heat fluxes are calculated using the model sea surface conditions, which differ from those applied to the JRA55 reanalysis. The first effect, however, should be negligible: JRA55-do primarily differs from JRA55 in the annual mean radiation, while their day-to-day variability—particularly the anomalous fields typically used in MHW analyses—remains largely consistent[67]. The negligibility of both effects is confirmed by reproducing Fig. 3 using the net heat flux from the ACCESS-OM2-01 output (Supplementary Fig. S10). The comparison shows that the temporal evolution of the temperature budget terms during MHWs dominated by different local drivers is broadly consistent, except for a higher proportion of ADV-dominated events, and a more prominent role of oceanic advection relative to "Other" in large-scale ADV-dominated MHWs (e.g. Supplementary Fig. S8d–e), consistent with more accurate calculation of fluxes related to model anomalies which are absent in JRA55. We therefore present the JRA55-based results in the main text, which allow decomposition of the heat flux components (e.g. Fig. 7) and some diagnostic properties like clouds, not available in JRA55-do.

It is important to note that the temperature budget is computed pixel-by-pixel for the entire dataset and then mapped to individual MHW entities based on their spatial footprints, rather than being calculated independently for each warm water mass as in ref[77]. As a result, this approach does not account for temperature changes due to MHW boundary movement. This approach, though not ideal, is necessary because MHWs are identified based on temperature anomalies. Consequently, their associated temperature budget diagnostics must also be expressed as anomalies. This becomes impractical when heat or water mass budgets are computed independently for each water mass. To our knowledge, all existing studies that apply heat (or temperature) budget analysis to evolving warm water masses define MHWs using fixed temperature thresholds, rather than seasonally varying anomaly fields[61,77]. Therefore, we first compute the temperature budget terms at each grid cell, remove the seasonal climatology to obtain anomalies, and then associate these anomalies with the corresponding MHW entities. This approach provides a succession of snapshot analyses of the local drivers influencing the pixels contained within each MHW object over its lifetime, rather than a complete Lagrangian temperature tendency budget that follows the evolving MHW entities. While not a purely Lagrangian analysis with closed budgets, our approach offers valuable insights into how local drivers evolve during MHW development and propagation.

Scaling MHWs in a spatiotemporal framework

Analysing MHW entities as sequences of moving objects from a composite perspective is substantially more challenging than interpreting fixed-grid MHW outputs, as each event exhibits distinct spatiotemporal dynamics,

with evolving shapes, sizes, and durations. To overcome this issue, we develop a normalisation method that scales the MHW entities in space and time so that they can be more directly compared. To compare the spatiotemporal evolution of individual MHWs, we normalise their shapes to fit within a unit circle (radius = 1) and standardise their durations from t = 0 (onset) to t = 1 (end). Specifically, we first compute the centroid (Supplementary Table S2) of each MHW at every time step and identify the maximum distance (r) from the centroid to its outermost boundary over the event's entire lifespan. Subsequently, we reposition each MHW by translating all grid points so that the centroid aligns with the origin, and scale spatial dimensions uniformly by a factor 1/r to constrain the maximum radius within unity. Pixels covered by lands remains blank in this and future composite processes. An example application of this technique is shown in Supplementary Fig. S11 (also animation version via https://github.com/ZijieZhaoMMHW/m_mhw1.0/blob/master/store_figure/tasmansea_example.gif), with four-day interval MHW object snapshots during the very intense and persistent 2015/16 Tasman Sea MHW. By applying these normalisation steps, each MHW is transformed into a standardised spatiotemporal structure contained within a unit cylinder. This uniform framework enables direct, meaningful comparisons of their shapes and dynamics, removing confounding differences in their original spatial scales and durations.

Characterising vertical structures of MHW entities

To characterise subsurface warming during the evolution in space and time of the MHW objects, while accounting for the influence of large vertical differences in temperature variability, we calculate the MHW severity index (SI)[78] for each vertical layer as:

$$SI = \frac{T - Clim}{Thre - Clim} \tag{2}$$

where T is daily ocean temperature, and $Clim$ and $Thre$ indicate the daily climatology and 90th percentile threshold, respectively, used to define MHWs. The depth-varying, spatially integrated SI is temporally interpolated according to the MHW lifetime and then composited to depict its vertical structure over the course of the MHW evolution. The resulting composites are subsequently normalised by their maximum values across depth to emphasise vertical variations during MHW development. Note that this procedure differs from that used to construct the evolution of MHW intensity (Fig. 5a), in which the spatially integrated MHW intensity is first temporally interpolated and normalised by the MHW lifetime and then composited.

Data availability

The model configuration of ACCESS-OM2 is publicly available at https://github.com/ACCESS-NRI/ACCESS-OM2. The JRA55 and JRA55-do reanalysis datasets can be obtained from the Japan Meteorological Agency at https://jra.kishou.go.jp/JRA-55/index_en.html. For this study, the datasets were retrieved and stored on Gadi, the supercomputing facility operated by Australia's National Computational Infrastructure. The output from ACCESS-OM2 can be accessed via https://doi.org/10.25914/608097cb3433f.

Code availability

Codes used to track and normalise MHW entities have been written up as a toolbox via github.com/ZijieZhaoMMHW/MHW_tracking. A Julia-based package is also under development and available at https://github.com/ZijieZhaoMMHW/Tracking_Julian. Both repositories will be actively maintained, with additional functions and usage examples to be added in future updates. Other codes for grid-cell MHW detection can be found via https://github.com/ZijieZhaoMMHW/m_mhw1.0, which is a MATLAB toolbox developed by the leading author (Z.Z.) for MHW analysis[79]. Codes to calculate offline mixed-layer temperature budgets can be found in https://github.com/ZijieZhaoMMHW/hbs. Some analyses in this study benefited from code provided by ref[80].

Received: 10 September 2025; Accepted: 12 February 2026
Published online: 26 February 2026

References

1. Hobday, A. J. et al. A hierarchical approach to defining marine heatwaves. *Prog. Oceanogr.* **141**, 227–238 (2016).
2. Oliver, E. C. et al. Marine heatwaves. *Annu. Rev. Mar. Sci.* **13**, 313–342 (2021).
3. Pearce A, Jackson G, Moore J, Feng M, Gaughan DJ. The "marine heat wave" off Western Australia during the summer of 2010/11. (2011).
4. Oliver, E. C. et al. Longer and more frequent marine heatwaves over the past century. *Nat. Commun.* **9**, 1324 (2018).
5. Capotondi, A. et al. A global overview of marine heatwaves in a changing climate. *Commun. Earth Environ.* **5**, 701 (2024).
6. Collins, M. et al. Extremes, abrupt changes and managing risks. In: *IPCC special report on the ocean and cryosphere in a changing climate*. (Cambridge University Press, 2022).
7. Deser, C. et al. Future changes in the intensity and duration of marine heat and cold waves: Insights from coupled model initial-condition large ensembles. *J. Clim.* **37**, 1877–1902 (2024).
8. Fox-Kemper, B. et al. Challenges and prospects in ocean circulation models. *Front. Mar. Sci.* **6**, 65 (2019).
9. Frölicher, T. L., Fischer, E. M. & Gruber, N. Marine heatwaves under global warming. *Nature* **560**, 360–364 (2018).
10. Xu, T. et al. An increase in marine heatwaves without significant changes in surface ocean temperature variability. *Nat. Commun.* **13**, 7396 (2022).
11. Oliver, E. C. Mean warming not variability drives marine heatwave trends. *Clim. Dyn.* **53**, 1653–1659 (2019).
12. England, M. H. et al. Drivers of the extreme North Atlantic marine heatwave during 2023. *Nature* https://doi.org/10.1038/s41586-025-08903-5 (2025).
13. Smale, D. A. et al. Marine heatwaves threaten global biodiversity and the provision of ecosystem services. *Nat. Clim. Chang.* **9**, 306–312 (2019).

14. Smith, K. E. et al. Global impacts of marine heatwaves on coastal foundation species. *Nat. Commun.* **15**, 5052 (2024).
15. Smith, K. E. et al. Biological impacts of marine heatwaves. *Annu. Rev. Mar. Sci.* **15**, 119–145 (2023).
16. Smith, K. E. et al. Socioeconomic impacts of marine heatwaves: Global issues and opportunities. *Science* **374**, eabj3593 (2021).
17. Wernberg, T. et al. Climate-driven regime shift of a temperate marine ecosystem. *Science* **353**, 169–172 (2016).
18. Wernberg, T. et al. An extreme climatic event alters marine ecosystem structure in a global biodiversity hotspot. *Nat. Clim. Chang.* **3**, 78–82 (2013).
19. Arias-Ortiz, A. et al. A marine heatwave drives massive losses from the world's largest seagrass carbon stocks. *Nat. Clim. Chang.* **8**, 338–344 (2018).
20. Whitney, F. A. Anomalous winter winds decrease 2014 transition zone productivity in the NE Pacific. *Geophys. Res. Lett.* **42**, 428–431 (2015).
21. Di Lorenzo, E. & Mantua, N. Multi-year persistence of the 2014/15 North Pacific marine heatwave. *Nat. Clim. Chang.* **6**, 1042–1047 (2016).
22. Smith, K. E. et al. Baseline matters: Challenges and implications of different marine heatwave baselines. *Prog. Oceanogr.* **231**, 103404 (2025).
23. Bonino, G., Masina, S., Galimberti, G. & Moretti, M. Southern Europe and western Asian marine heatwaves (SEWA-MHWs): A dataset based on macroevents. *Earth Syst. Sci. Data* **15**, 1269–1285 (2023).
24. Prochaska, J. X., Beaulieu, C. & Giamalaki, K. The rapid rise of severe marine heat wave systems. *Environmental Research: Climate* **2**, 021002 (2023).
25. Ren, J., Wang, C. & Yao, Y. Spatiotemporally continuous marine heatwaves: A novel clustering approach reveals increasing frequency, duration, area, intensity, and movement distance. *Geophys. Res. Lett.* **52**, e2024GL113211 (2025).
26. Scannell, H. et al. Spatiotemporal evolution of marine heatwaves globally. *J. Atmos. Ocean. Technol.* **41**, 1247–1263 (2024).
27. Sun, D., Jing, Z., Li, F. & Wu, L. Characterizing global marine heatwaves under a spatio-temporal framework. *Prog. Oceanogr.* **211**, 102947 (2023).
28. Holbrook, N. J. et al. A global assessment of marine heatwaves and their drivers. *Nat. Commun.* **10**, 2624 (2019).
29. Chapman, C. C., Sloyan, B. M., Moore, T. S., Reilly, J. A. & Matear, R. J. Marine heatwaves in the East Australian Current modulated by mesoscale eddies. *J. Geophys. Res. Oceans* **130**, e2024JC021395 (2025).
30. Elzahaby, Y., Schaeffer, A., Roughan, M. & Delaux, S. Oceanic circulation drives the deepest and longest marine heatwaves in the East Australian Current system. *Geophys. Res. Lett.* **48**, e2021GL094785 (2021).
31. Li, J., Roughan, M. & Hemming, M. Interactions between cold cyclonic eddies and a western boundary current modulate marine heatwaves. *Commun. Earth Environ.* **4**, 380 (2023).
32. Li, J., Roughan, M. & Kerry, C. Drivers of ocean warming in the western boundary currents of the Southern Hemisphere. *Nat. Clim. Chang.* **12**, 901–909 (2022).
33. Li, J., Roughan, M. & Kerry, C. Variability and drivers of ocean temperature extremes in a warming western boundary current. *J. Clim.* **35**, 1097–1111 (2022).
34. Perkins-Kirkpatrick. S. et al. The role of natural variability and anthropogenic climate change in the 2017/18 Tasman Sea marine heatwave (2019).
35. Salinger, M. J. et al. The unprecedented coupled ocean-atmosphere summer heatwave in the New Zealand region 2017/18: Drivers, mechanisms and impacts. *Environ. Res. Lett.* **14**, 044023 (2019).
36. Shears, N. T., Bowen, M. M. & Thoral, F. Long-term warming and record-breaking marine heatwaves in the Hauraki Gulf, northern New Zealand. *N. Z. J. Mar. Freshw. Res.* https://doi.org/10.1080/00288330.2024.2319100 (2024).
37. Bian, C. et al. Oceanic mesoscale eddies as crucial drivers of global marine heatwaves. *Nat. Commun.* **14**, 2970 (2023).
38. Vogt, L., Burger, F. A., Griffies, S. M. & Frölicher, T. L. Local drivers of marine heatwaves: A global analysis with an earth system model. *Front. Clim.* **4**, 847995 (2022).
39. Zhao, Z., Holbrook, N. J. & Oliver, E. C. An eddy pathway to marine heatwave predictability off eastern Tasmania. *Front. Clim.* **4**, 907828 (2022).
40. Bian, C., Jing, Z., Wang, H. & Wu, L. Scale-dependent drivers of marine heatwaves globally. *Geophys. Res. Lett.* **51**, e2023GL107306 (2024).
41. Gregory, C. H., Holbrook, N. J., Marshall, A. G. & Spillman, C. M. Atmospheric drivers of Tasman Sea marine heatwaves. *J. Climate* **36**, 5197–5214 (2023).
42. Li, Z., Holbrook, N. J., Zhang, X., Oliver, E. C. & Cougnon, E. A. Remote forcing of Tasman Sea marine heatwaves. *J. Climate* **33**, 5337–5354 (2020).
43. Oliver, E. C. et al. The unprecedented 2015/16 Tasman Sea marine heatwave. *Nat. Commun.* **8**, 16101 (2017).
44. Ridgway K, Hill K. The East Australian Current. In *Marine Climate Change in Australia: Impacts and Adaptation Responses 2009 Report Card*, 16 (2009).
45. Sala, J., Giglio, D., Capotondi, A., Sukianto, T. & Kuusela, M. Leading dynamical processes of global marine heatwaves in an ocean state estimate. *Ocean Sci.* **21**, 2463–2479 (2025).
46. Marin, M., Feng, M., Bindoff, N. L. & Phillips, H. E. Local drivers of extreme upper ocean marine heatwaves assessed using a global ocean circulation model. *Front. Clim.* **4**, 788390 (2022).
47. Oke, P. R. et al. Revisiting the circulation of the East Australian Current: Its path, separation, and eddy field. *Prog. Oceanogr.* **176**, 102139 (2019).
48. Ypma, S. L., van Sebille, E., Kiss, A. E. & Spence, P. The separation of the E ast A ustralian C urrent: AL agrangian approach to potential vorticity and upstream control. *J. Geophys. Res. Oceans* **121**, 758–774 (2016).
49. Stevens, C. L., O'Callaghan, J. M., Chiswell, S. M. & Hadfield, M. G. Physical oceanography of New Zealand/Aotearoa shelf seas–a review. *N. Z. J. Mar. Freshw. Res.* **55**, 6–45 (2021).
50. Tilburg, C. E., Hurlburt, H. E., O'Brien, J. J. & Shriver, J. F. The dynamics of the East Australian current system: The Tasman front, the East Auckland current, and the East Cape current. *J. Phys. Oceanogr.* **31**, 2917–2943 (2001).
51. Malan, N. et al. Lifting the lid on marine heatwaves. *Prog. Oceanogr.* https://doi.org/10.1016/j.pocean.2025.103539 (2025).
52. Zhang, Y., Du, Y., Feng, M. & Hobday, A. J. Vertical structures of marine heatwaves. *Nat. Commun.* **14**, 6483 (2023).
53. Sun, D., Li, F., Jing, Z., Hu, S. & Zhang, B. Frequent marine heatwaves hidden below the surface of the global ocean. *Nat. Geosci.* **16**, 1099–1104 (2023).
54. Yu, J., Zhang, H., Wang, P., Lu, F. & Ning, J. A geospatial skeleton framework for unveiling the 3D structure and dynamics of marine heatwaves from earth observation data. *Geo-spatial Inf. Sci.* 1–16 (2025).
55. Hauri, C. et al. More than marine heatwaves: A new regime of heat, acidity, and low oxygen compound extreme events in the Gulf of Alaska. *AGU Adv.* **5**, e2023AV001039 (2024).
56. Li, C. et al. The ocean losing its breath under the heatwaves. *Nat. Commun.* **15**, 6840 (2024).
57. Burger, F. A., Terhaar, J. & Frölicher, T. L. Compound marine heatwaves and ocean acidity extremes. *Nat. Commun.* **13**, 4722 (2022).
58. Amaya, D. J., Miller, A. J., Xie, S.-P. & Kosaka, Y. Physical drivers of the summer 2019 North Pacific marine heatwave. *Nat. Commun.* **11**, 1903 (2020).
59. Kajtar, J. B., Bachman, S. D., Holbrook, N. J. & Pilo, G. S. Drivers, dynamics, and persistence of the 2017/2018 Tasman Sea marine heatwave. *J. Geophys. Res. Oceans* **127**, e2022JC018931 (2022).

60. Zhang, W., Zhao, Z., Hobday, A. J. & Holbrook, N. J. Global diversity of marine heatwave evolutions. *Geophys. Res. Lett.* **52**, e2025GL117516 (2025).
61. Bailey, S. T., Drake, H. F., Gruenburg, L. K., Abernathey, R. P. & Torres, M. I. The thermodynamics of the 2023 Gulf of Mexico Marine heatwave. *Geophys. Res. Lett.* **52**, e2024GL111768 (2025).
62. Spillman, C. M. et al. What makes a marine heatwave forecast useable, useful and used?. *Prog. Oceanogr.* **234**, 103464 (2025).
63. Kobayashi, S. et al. The JRA-55 reanalysis: General specifications and basic characteristics. *J. Meteorol. Soc. Jpn. Ser. II* **93**, 5–48 (2015).
64. Harada, Y. et al. The JRA-55 reanalysis: Representation of atmospheric circulation and climate variability. *J. Meteorol. Soc. Jpn. Ser. II* **94**, 269–302 (2016).
65 Kiss, A. E. et al. ACCESS-OM2 v1.0: A global ocean–sea ice model at three resolutions. *Geosci. Model Dev.* **13**, 401–442 (2020).
66. Solodoch, A. et al. How does Antarctic bottom water cross the Southern Ocean?. *Geophys. Res. Lett.* **49**, e2021GL097211 (2022).
67. Tsujino, H. et al. JRA-55 based surface dataset for driving ocean–sea-ice models (JRA55-do). *Ocean Model* **130**, 79–139 (2018).
68. Marin, M., Bindoff, N. L., Feng, M. & Phillips, H. E. Slower long-term coastal warming drives dampened trends in coastal marine heatwave exposure. *J. Geophys. Res. Oceans* **126**, e2021JC017930 (2021).
69. Pilo, G. S., Holbrook, N. J., Kiss, A. E. & Hogg, A. M. Sensitivity of marine heatwave metrics to ocean model resolution. *Geophys. Res. Lett.* **46**, 14604–14612 (2019).
70. Wang, Y., Holbrook, N. J. & Kajtar, J. B. Predictability of marine heatwaves off Western Australia using a linear inverse model. *J. Climate* **36**, 6177–6193 (2023).
71. Hayashida, H., Matear, R. J., Strutton, P. G. & Zhang, X. Insights into projected changes in marine heatwaves from a high-resolution ocean circulation model. *Nat. Commun.* **11**, 4352 (2020).
72. Banzon, V., Smith, T. M., Chin, T. M., Liu, C. & Hankins, W. A long-term record of blended satellite and in situ sea-surface temperature for climate monitoring, modeling and environmental studies. *Earth Syst. Sci. Data* **8**, 165–176 (2016).
73. Reynolds, R. W. et al. Daily high-resolution-blended analyses for sea surface temperature. *J. Climate* **20**, 5473–5496 (2007).
74. Moisan, J. R. & Niiler, P. P. The seasonal heat budget of the North Pacific: Net heat flux and heat storage rates (1950–1990). *J. Phys. Oceanogr.* **28**, 401–421 (1998).
75. Stevenson, J. W. & Niiler, P. P. Upper ocean heat budget during the Hawaii-to-Tahiti shuttle experiment. *J. Phys. Oceanogr.* **13**, 1894–1907 (1983).
76. Paulson, C. A. & Simpson, J. J. Irradiance measurements in the upper ocean. *J. Phys. Oceanogr.* **7**, 952–956 (1977).
77. Drake, H. F. et al. Water mass transformation budgets in finite-volume generalized vertical coordinate ocean models. *J. Adv. Model. Earth Syst.* **17**, e2024MS004383 (2025).
78. Sen Gupta, A. et al. Drivers and impacts of the most extreme marine heatwave events. *Sci. Rep.* **10**, 19359 (2020).
79. Zhao, Z. & Marin, M. A. A MATLAB toolbox to detect and analyze marine heatwaves. *J. Open Source Softw.* **4**, 1124 (2019).
80. Greene, C. A. et al. The climate data toolbox for MATLAB. *Geochem. Geophys. Geosyst.* **20**, 3774–3781 (2019).

Acknowledgements

NJH acknowledges support from the ARC Centre of Excellence for Climate Extremes (CE170100023). This manuscript was conceived and initially developed as part of the ARC Centre of Excellence for Climate Extremes funded workshop entitled "Definition, Dynamics and Predictability of Marine Heatwaves" held from 23-25 May 2023 at Moreton Island, Queensland, Australia. The workshop goals and activities also contribute to the CLIVAR Research Focus on Marine Heatwaves in the Global Ocean and the International Commission on Climate of IAMAS/IUGG. SC was supported by the HEAT project (funded by Fonds Pacifique) and the MaHeWa project (ANR-23-POCE-0001, funded by Agence Nationale de la Recherche under the France 2030 program). ASG is supported by an ARC Future Fellowship (FT220100475). AC was supported by the NOAA Climate Program Office Climate Variability and Predictability Program Awards # NA24OARX431C0024-T1-01 and NA24OARX431C0021. This work was supported by computational resources provided by the Australian Government through the National Computational Infrastructure (NCI) under the National Computational Merit Allocation Scheme and ANU Merit Allocation Scheme. We thank the vibrant community of the Consortium for Ocean–Sea Ice Modelling in Australia (COSIMA; cosima.org.au) for making the ACCESS-OM2 outputs and analysis tools available through the NCI. COSIMA and AEK are funded through the Australian Research Council grant LP200100406. Z.Z. thanks Di Sun (Ocean University of China) for making her MATLAB code for MHW tracking publicly available at https://github.com/cindyisok/MHWTracking, and for valuable discussions.

Author contributions

N.J.H., A.C., S.C., and J.B.K. conceptualized the study. Z.Z. designed the methodology and performed the analysis. Z.Z. and N.J.H. drafted the initial manuscript. S.C., J.B.K., A.S.G., E.B., M.A.D., M.F., A.E.K., and C. M. S. contributed to interpreting the results and reviewing and editing the manuscript. All authors reviewed the manuscript and approved the submission.

Funding

This project was funded by the ARC Centre of Excellence for Climate Extremes (CE170100023). SC also received funding from the HEAT project (Fonds Pacifique) and the MaHeWa project (ANR-23-POCE-0001, Agence Nationale de la Recherche, France 2030 program). ASG was also funded by an ARC Future Fellowship (FT220100475). AEK was also funded through the Australian Research Council grant LP200100406. AC was supported by the NOAA Climate Program Office Climate Variability and Predictability Program Awards # NA24OARX431C0024-T1-01 and NA24OARX431C0021.

Declarations

Competing interests

The authors declare no competing interests.

Additional information

Supplementary Information The online version contains supplementary material available at https://doi.org/1

0.1038/s41598-026-40354-4.

Correspondence and requests for materials should be addressed to N.J.H.